Computational Simulations of Microscale Shock-Vortex Interaction

Using a Mixed Discontinuous Galerkin Method

H. Xiao and R.S. Myong

Department of Aerospace and System Engineering and Research Center for Aircraft Parts Technology,

Gyeongsang National University, Jinju, Gyeongnam, 660-701, South Korea

myong@gnu.ac.kr

Abstract: This study extensively investigates the physics of microscale shock-vortex interaction of argon gas by solving conservation laws with non-Newtonian constitutive relations. In order to solve the conservation laws and associated implicit type constitutive equations of viscous stress and heat flux numerically, a mixed discontinuous Galerkin (DG) formulation is developed. Three major characteristics are found in the microscale shock-vortex interaction in thermal nonequilibrium: the absence of quadrupolar acoustic wave structure, which is the major feature in macroscale near-equilibrium; the increase in the dissipation rate during the strong interaction; and the decrease in enstrophy during the weak interaction. Moreover, we show that the strong shock-vortex interaction in high shock or vortex Mach numbers can cause an increase in enstrophy. We also find the viscous effect to be dominant in the net vorticity generation. Among shock and vortex parameters, the shock Mach number, vortex Mach number and vortex size turn out to play a critical role in the deformation of the vortex and the strength of interaction, which in turn govern the net viscous vorticity generation, the change in the dissipation rate and the increase or decrease in enstrophy during the interaction.

Keywords: CFD, microscale shock-vortex interaction, mixed discontinuous Galerkin method

1 Introduction

Shock-vortex interactions have been extensively investigated in the past decades because they can provide fundamental knowledge on flow physics of high speed gas flows. The shock wave and the vortex are deformed and/or disrupted during the interaction, and it alters or destroys the shock wave and the vortex structure. Most of the previous studies on this problem have been conducted for the purpose of understanding the noise production mechanism and deformation of the shock wave and vortex. Since thermal nonequilibrium effects are in general negligible at the macroscale, virtually all the previous studies are based on compressible Euler or Navier-Stokes-Fourier (NSF) equations [1-6], which are derived from the Boltzmann equation with the assumption of near-thermal-equilibrium, for analyzing the physical phenomena.

Previous computational investigations showed that strong shock-vortex interactions cause significant shock deformation and result in the formation of secondary shock structures [1]. Subsequently, Inoue and Hattori [3] predicted that a third sound wave was generated in the interaction of an initially planar shockwave and a single vortex. Later, Zhang and Shu [7] reported that additional sound waves would be generated in the subsequent secondary (and tertiary) interactions involving reflected shocks, shock lets, and the deformed vortex. In addition, Chatterjee and Vijayaraj [8] captured multiple acoustic waves, quadrupolar in nature and with successive layout of phase. The number of acoustic waves captured was more than the maximum of three reported in previous studies. The additional sound waves are due to acoustic addition from the rotating elliptical vortex following the interaction. Chang, Barik and Chang [9] study various cases of shock-vortex interactions. These studies found that the most remarkable flow elements of the shock-vortex interaction are the induced expansion wave and shock wave.

Although numerous computational studies have been conducted on the shock-vortex interaction at the macroscale, the microscale shock-vortex interaction in thermal nonequilibrium is not yet well understood. Up to now, only a few microscale cases involving limited Mach and Knudsen numbers have been conducted by Koffi et al. using direct simulation Monte Carlo (DSMC) [10-11]. That study

showed that, within the range of the parameters considered, the viscous attenuation of the vortex was found to dominate the gas flow in the microscale shock-vortex interaction. At microscale, the attenuation overwhelmed the enstrophy generation, which is in stark contrast to the enstrophy production in the macroscale shock-vortex interaction. However, critical questions of the microscale shock-vortex interaction, including whether enstrophy attenuation persists at higher shock and vortex Mach numbers or a larger vortex, remain unsolved.

At the microscale, the gas flow regimes are determined by the local Knudsen number, which is defined as the ratio of the mean free path to the characteristic length. In the present microscale shock-vortex interaction with local Knudsen numbers falling in the non-continuum transitional flow regime, the use of the NSF model based on a linear framework becomes questionable. The DSMC developed by Bird [12] is the most popular method that can be used in the rarefied and microscale gas flows [13]. On the other hand, our study introduces a new computational model based on a nonlinear coupled non-Newtonian frame work to more efficiently investigate compressible shock-vortex interactions at the microscale for a far greater range of shock and vortex parameters than in the previous studies. In order to solve the highly nonlinear continuum-based implicit model numerically, the mixed discontinuous Galerkin (DG) formulation is employed. In the new model consisting of the conservation laws and nonlinear coupled constitutive relations (NCCR), the relationship of viscous stress and thermal conduction is expressed in terms of implicit nonlinear coupled algebraic functions of the velocity and temperature gradients [14]. Extensive validation studies of the phenomenological nonlinear coupled model had been conducted by investigating the compressive shock dominated gas flows [14-18] and the velocity-shear dominated force-driven Poiseuille gas flow [19]. The present shock-vortex interaction study may be regarded as the first computational attempt of investigating the strong interaction of two important thermal nonequilibrium phenomena on the basis of continuum high order constitutive equations; compressive shock structure and velocity-shear of the vortex.

The investigation in this work involves detailed computational study of the dynamics at vortex radial length scales on the order of the shock thickness. It is well known that high-order methods are critical for resolving shock wave interactions. Shock-fitting algorithms have also been developed as

an alternative and can achieve uniform high-order accuracy [20-21]. However, a shock-capturing method coupled with the mixed DG method is used in this work owing to its relatively simple implementation and shock capturing capability. By extending previous three cases treated by the DSMC, interactions of up to Mach 3.5 shock waves with supersonic or subsonic vortex, 90 cases in total, are examined in much greater detail.

This paper is organized as follows. Sec. 2 presents physical system of the microscale shock-vortex interaction. Subsequently, a computational method based on the mixed DG formulation for the two dimensional conservation laws and NCCR model for argon gas is described. In Sec. 3 we present the validation results of the DG method for NSF and NCCR models. In Sec.4, by studying extensive cases of microscale shock-vortex interaction, different vortex deformation behaviors through a shock are found. Furthermore, we study the overall dynamics of net production and the dissipation of vorticity in detail. In Sec. 5, the effects of interaction parameters on the microscale shock-vortex interaction are examined. Finally, conclusions and remarks are given in Sec. 6.

2 Physical system and computational method

2.1 Physical system

The physical system of the two-dimensional microscale shock-vortex interaction is shown in Fig.1. In the case of a moving shock instead of a standing shock, start-up errors might exist. However, in order to compare with previous DSMC results obtained by Koffi et al. [10-11], a moving shock and a stationary vortex are considered in the present simulation. A microscale discrete vortex is formed by prescribing its initial flow to be that of a composite vortex [9,11,22]. The physical size of the composite vortex in area is about one-fourth that of a Taylor-type vortex with the same core size. It is chosen for its computational advantages. The rotation center of the vortex is initially stationary and a velocity distribution between a core radius ($r = r_1$) and an outer radius ($r = r_2$) is prescribed for the vortex.

In this physical system, the maximum tangential velocity is found at the core radius. Inside the core ($r < r_1$), the velocity goes linearly to zero at $r = 0$. Outside r_2 ($r > r_2$), the tangential velocity is set to zero. The tangential velocity distribution is as follows,

$$V_\theta(r) = \begin{cases} \dfrac{V_c}{r_1} r & r \leq r_1 \\ Ar + \dfrac{B}{r} & r_1 \leq r \leq r_2 \\ 0 & r > r_2 \end{cases} \tag{2.1}$$

where

$$A = -\frac{V_c r_1}{r_2^2 - r_1^2} \ , \quad B = \frac{V_c r_2^2 r_1}{r_2^2 - r_1^2} \ , \quad V_c = a M_v.$$

Here a, V_c, and M_V represent the local speed of sound, the maximum tangential velocity, and the vortex Mach number, respectively.

The temperature and pressure in the quiescent field surrounding the vortex are prescribed. Inside the vortex, pressure, density, and energy are determined by balancing the pressure gradients with the centripetal force, which is equivalent to solving the following system,

$$\frac{dp}{dr} = \frac{\rho V_\theta}{r}, \ p = \rho RT, \ \frac{p}{\rho^\gamma} = \text{constant}.$$

Rectangular 200×200 grids are used for defining the computational domain. The monatomic gas considered in the computational simulations is assumed argon, and its initial quiescent state surrounding the vortex has a pressure of 1,013 Pa and a temperature of 273K. For this initial condition, the mean free path is $\lambda = 6.26 \times 10^{-6} m$. In our simulations, the composite vortex outer radius is double of the size of the core radius.

2.2 Computational Method

2.2.1 Mixed DG scheme for the two dimensional conservation laws

5

After the following dimensionless variables are introduced,

$$t^* = t/(L/u_r),\ x^* = x/L,\ \eta^* = \eta/\eta_r,\ k^* = k/k_r,\ \mathbf{u}^* = \mathbf{u}/u_r,\ \rho^* = \rho/\rho_r,\ T^* = T/T_r,$$

$$p^* = p/p_r,\ E^* = E/u_r^2,\ \mathbf{\Pi}^* = \mathbf{\Pi}/(\eta_r u_r/L),\ \mathbf{Q}^* = \mathbf{Q}/(k_r \Delta T/L),$$

where the subscript r represents the reference state (for example, the condition before the shockwave), the non-dimensional conservation laws for monatomic gas flows (with the asterisks omitted for notational brevity) can be written as [14,15,23],

$$\frac{\partial \mathbf{U}}{\partial t} + \nabla \cdot \mathbf{F}_{\text{inv}}(\mathbf{U}) + \nabla \cdot \mathbf{F}_{\text{vis}}(\mathbf{U}) = 0, \tag{2.2}$$

where conservative and flux variables are defined as,

$$\mathbf{U} = \begin{pmatrix} \rho \\ \rho\mathbf{u} \\ \rho E \end{pmatrix}, \mathbf{F}_{\text{inv}}(\mathbf{U}) = \begin{pmatrix} \rho\mathbf{u} \\ \rho\mathbf{uu} + \dfrac{1}{\gamma M^2} p\mathbf{I} \\ \left(\rho E + \dfrac{1}{\gamma M^2} p\right)\mathbf{u} \end{pmatrix}, \mathbf{F}_{\text{vis}}(\mathbf{U}, \nabla\mathbf{U}) = \frac{1}{\text{Re}} \begin{pmatrix} 0 \\ \mathbf{\Pi} \\ \mathbf{\Pi}\cdot\mathbf{u} + \dfrac{1}{\text{Ec Pr}}\mathbf{Q} \end{pmatrix}.$$

Here ρ is the mass density, $\mathbf{u}$ is the fluid velocity, p is the pressure, T is the gas temperature, E is the total energy density, $\mathbf{\Pi}$ is the shear stress, $\mathbf{Q}$ is the heat flux, and $\mathbf{I}$ denotes the unit second-rank tensor. The η, k are the Chapman-Enskog shear viscosity and thermal conductivity, respectively. The M, Re, Ec and Pr are dimensionless gas dynamic parameters: Mach, Reynolds, Eckert, and Prandtl numbers, respectively:

$$M = \frac{u_r}{(\gamma R T_r)^{1/2}},\ \ \text{Re} = \frac{\rho_r u_r L}{\eta_r},\ \ \text{Ec} = (\gamma - 1)M^2,\ \ \text{Pr} = \frac{C_{pr}\eta_r}{k_r},$$

where C_p denotes the heat capacity per mass at a constant pressure. In present work, the speed of sound of argon gas before the shock wave is chosen as the reference velocity u_r, resulting in $M=1$. Nonetheless, we will keep the reference Mach number M in the equations in order to show its role in the formulation. Also the core radius of the vortex r_1 is used for the reference length L. For the conventional linear uncoupled Newtonian model, the constitutive relations are defined as follows，

$$\mathbf{\Pi} = -2\eta\left[\nabla\mathbf{u}\right]^{(2)},\ \ \mathbf{Q} = -k\nabla T,$$

where the symbol $[\ ]^{(2)}$ denotes the traceless symmetric part of the second-rank tensor. In the dimensionless expression, the viscosity and the conductivity can be written as

$$\eta = T^s, \ k = T^s,$$

where $s = 0.75$ is used for the argon molecule.

Bassi and Rebay [24] introduced a mixed formulation for the treatment of the second-order viscous terms to solve the Navier–Stokes equations, which differs from the conventional DG method [25-27]. The formulation introduces auxiliary variables to resolve the governing equations as a first-order coupled system for the local DG approach. In this work, an auxiliary variable **S** is introduced to be the derivatives of the conserved variables **U**, setting S(**U**)=$T^s \nabla$ **U**. Then a coupled system for **S** and **U** can be derived as

$$\begin{cases} \mathbf{S(U)} = T^s \nabla \mathbf{U}, \\ \dfrac{\partial \mathbf{U}}{\partial t} + \nabla \cdot \mathbf{F}_{inv}(\mathbf{U}) + \nabla \cdot \mathbf{F}_{vis}(\mathbf{U,S}) = 0. \end{cases} \tag{2.3}$$

The spatial derivatives of primitive variables such as u_x is then computed by expanding the derivatives of the conservable variables, for example $T^s u_x = (1/\rho)[T^s(\rho u)_x - T^s \rho_x u]$. Constitutive relations for the two models are expressed as follows: for the NSF model $(\mathbf{\Pi}, \mathbf{Q}) = f_{linear}(\mathbf{S}\ (\mathbf{U}))$, and for the NCCR model $(\mathbf{\Pi}, \mathbf{Q})_{NCCR} = f_{nonlinear}(\mathbf{S}\ (\mathbf{U}), p, T)$. Note that the introduction of an auxiliary variable such as one in (2.3) is necessary for the nonlinear *implicit* type NCCR constitutive model.

The computational domain contains 200×200 elements (cells) that are equally spaced. In order to discretize the coupled system (2.3), the numerical solutions of **U** and **S** are approximated by $\mathbf{U}_h$ and $\mathbf{S}_h$ in the j ($1 \leq j \leq 200 \times 200$) element, respectively,

$$\mathbf{U}_h(x,y,t) = \sum_{i=1}^{K} \mathbf{U}_j^i(t)\varphi^i(x,y), \ \ \mathbf{S}_h(x,y,t) = \sum_{i=1}^{K} \mathbf{S}_j^i(t)\varphi^i(x,y),$$

where $\varphi^i(x,y)$ is a genuine two-dimensional polynomial basis of the order of approximation I. K and I are related by [26]

$$K = \frac{(I+1)(I+2)}{2}.$$

7

Here, we use P^2 approximation, meaning I=2 and K=6. In this study, the scaled Legendre basis functions are adopted for the function φ.

$$\varphi^1 = 1, \varphi^2 = x^*, \varphi^3 = y^*, \varphi^4 = x^{*2} - \frac{1}{3}, \varphi^5 = x^* y^*, \varphi^6 = y^{*2} - \frac{1}{3},$$

where $x^* = \dfrac{x - x_o}{\Delta x / 2}$, $y^* = \dfrac{y - y_o}{\Delta y / 2}$. The x_o, y_o are the coordinates at the center of local mesh, and $\Delta x, \Delta y$ are the local mesh sizes. The basis functions are defined in global sense, meaning that the same basis functions are used in each local mesh. The coupled system (2.3) is multiplied by the basis function φ and then integrated by parts for derivative terms over element Ω, and the weak formulation of the coupled system can be derived to find $\mathbf{U}_h$ and $\mathbf{S}_h$

$$\begin{cases} \int_\Omega \mathbf{S}\boldsymbol{\varphi} dV + \int_\Omega T^s \nabla \boldsymbol{\varphi} \mathbf{U} dV - \int_\Gamma T^s \boldsymbol{\varphi} \mathbf{U} ds = 0, \\ \dfrac{\partial}{\partial t} \int_\Omega \mathbf{U}\boldsymbol{\varphi} dV - \int_\Omega \nabla \boldsymbol{\varphi} \mathbf{F}_{inv} dV + \int_\Gamma \boldsymbol{\varphi} \mathbf{F}_{inv} ds - \int_\Omega \nabla \boldsymbol{\varphi} \mathbf{F}_{vis} dV + \int_\Gamma \boldsymbol{\varphi} \mathbf{F}_{vis} ds = 0, \end{cases}$$

(2.4)

where Γ denotes the boundaries of the element Ω.

The equations of auxiliary unknowns are resolved first to compute the derivatives of conservative variables in which the variable $\eta(x, y, t)$ is updated at each time step. The boundary integrals of each element are replaced by a numerical flux function as follows. For inviscid terms, the local Lax-Friedrichs (LxF) flux, $\mathbf{h}_{inv}$, is applied:

$$\mathbf{h}_{inv}(\mathbf{U}^-, \mathbf{U}^+, \mathbf{n}) = \frac{1}{2}\left[\mathbf{F}_{inv}(\mathbf{U}^-) + \mathbf{F}_{inv}(\mathbf{U}^+) - C(\mathbf{U}^+ - \mathbf{U}^-) \right], \text{ where } C = \max\left(\left| u^- \right| + \frac{a^-}{M}, \left| u^+ \right| + \frac{a^+}{M} \right),$$

where $a = T^{1/2}$ is the non-dimensional speed of sound at the control volume interface. The signs – and + denote the insides and outsides of an elemental interface. The Mach number M in a/M instead of a appears in the formulation of the coefficient C from the characteristic speed in dimensionless form. The central flux is applied to the remaining boundary integrals. For the viscous term,

$$\mathbf{h}_{vis}(\mathbf{U}^-, \mathbf{S}^-, \mathbf{U}^+, \mathbf{S}^+; \mathbf{n}) \cong \int_\Gamma \boldsymbol{\varphi} \mathbf{F}_{vis} dx = \frac{1}{2}\left[\mathbf{F}_{vis}(\mathbf{U}^-, \mathbf{S}^-) + \mathbf{F}_{vis}(\mathbf{U}^+, \mathbf{S}^+) \right],$$

and for terms in the auxiliary unknown equations,

$$\mathbf{h}_{\text{aux}}(\mathbf{U}^-, \mathbf{U}^+; \mathbf{n}) \cong \int_\Gamma T^s \boldsymbol{\varphi} \mathbf{U} dx = \frac{1}{2}\left[T^{s-}\mathbf{U}^- + T^{s+}\mathbf{U}^+\right].$$

The volume integrals within the element Ω are resolved by the Gaussian quadrature with nine Gaussian points. Finally, the coupled system (2.4) can be written in semi-discrete form as

$$\mathbf{LS} = \mathbf{R}_S(\mathbf{U}),$$

$$\mathbf{L}\frac{\partial \mathbf{U}}{\partial t} = \mathbf{R}_U(\mathbf{U}),$$

which can be solved by the fourth-order Runge-Kutta time integration. Owing to the orthogonal property of basis functions, the diagonal matrix $\mathbf{L}$ is readily invertible.

In the initial condition, the coefficients of conservation variables are specified on the basis of upstream or downstream of the shock wave;

$$\mathbf{U}_j^1(t=0)=\mathbf{U}_{\text{up,down,vortex}}, \ \mathbf{U}_j^i(t=0)=0 \ (i=2,\cdots,6).$$

The coefficients of auxiliary unknown are set to zero:

$$\mathbf{S}_j^i(t=0)=0 \ (i=1,\cdots,6).$$

The time step Δt is computed as [26]

$$\Delta t = \min(\Delta t_1, \Delta t_2), \ \Delta t_1 = \frac{1}{(I+1)^2}\frac{\Delta x \ \text{CFL}}{|u|+\dfrac{a}{M}+\dfrac{\eta}{\Delta x}}, \ \Delta t_2 = \frac{1}{(I+1)^2}\frac{\Delta y \ \text{CFL}}{|u|+\dfrac{a}{M}+\dfrac{\eta}{\Delta y}},$$

where CFL is the Courant-Friedrichs-Lewy condition.

For a single simulation run, about two hours on 64 bit Intel(R) Core(TM) i7-2600 CPU are required to have converged solutions. Numerical computations studied so far indicated that the computing time of the DG-NCCR code is comparable to that of the DG-NSF code. The only excess load, which is caused by the addition of few iterations (less than 10 in most cases) when the stress and heat flux are calculated from the implicit algebraic constitutive equations, occupies a small fraction of computing time in the code (about 30 percent).

2.2.2 Numerical boundary conditions and limiter

As shown in Fig.1, the right boundary of the computational domain is defined as the condition before the shock wave while the left boundaries defined as the condition after the shock wave. Numerical boundary condition at the right boundary is set by the stationary condition before the shock wave. Numerical boundary condition at the left boundary is set by the moving shock Mach number and associated thermodynamic condition specified by the Rankine-Hugoniot relations. These are basically similar to DSMC work [11]. Furthermore, $\mathbf{U}_j^i(t)=0$ (i=2,$\cdots$,6) is set in DG implementation, since the flow condition is assumed constant at the boundary cells. The upper and lower boundaries are set according to the flow condition; before and after the shock wave. Since the shock wave is moving, the upper and lower boundaries are updated in every time step.

A high order slope limiter and shock detection [26] are adopted for the present DG scheme. The limiter is applied to eliminate oscillations in the shock simulations. The components of $\mathbf{U}$ can be limited as follows:

$$\tilde{\mathbf{U}}_j^m = \min \mathrm{mod}\left(\mathbf{U}_j^m,\ \mathbf{U}_{j+1}^1 - \mathbf{U}_j^1,\ \mathbf{U}_j^1 - \mathbf{U}_{j-1}^1\right)(m=2,3)$$

with the min mod function

$$\min \mathrm{mod}\left(d_1,d_2,d_3\right) = \begin{cases} (\mathrm{sgn})\min\left(|d_1|,|d_2|,|d_3|\right) & \text{if } \mathrm{sgn} = \mathrm{sgn}\,d_1 = \mathrm{sgn}\,d_2 = \mathrm{sgn}\,d_3, \\ 0 & \text{otherwise.} \end{cases}$$

The shock detection is implemented into the DG scheme as follows;

$$\mathrm{D}_j = \frac{\left|\int_{\partial \mathrm{I}_j} \left(\mathbf{U}_j - \mathbf{U}_{\mathrm{nbj}}\right) d\Gamma\right|}{\Delta x^{(\mathrm{I}+1)/2}\left|\partial \mathrm{I}_j^-\right|\left\|\mathbf{U}_j\right\|},$$

where $\mathbf{U}_{\mathrm{nbj}}$ indicates the neighboring element of $\mathbf{U}_j$ with a common boundary $\partial \mathrm{I}_j^-$, and //$\mathbf{U}_j$// is the norm of $\mathbf{U}_j$. The discontinuity detection scheme can be summarized as follows:

$$\begin{cases} \text{If } \mathrm{D}_j > 1 \Rightarrow \mathbf{U}_h \text{ is discontinuous,} \\ \text{If } \mathrm{D}_j < 1 \Rightarrow \mathbf{U}_h \text{ is smooth.} \end{cases}$$

2.2.3 NCCR for modeling gas flows in thermal nonequilibrium

For the NCCR model, $(\mathbf{\Pi}, \mathbf{Q})_{\text{NCCR}} = \text{f}_{\text{non-linear}}(\mathbf{S}(\mathbf{U}), p, T)$, the relationship of $\mathbf{\Pi}$ and $\mathbf{Q}$ is expressed in terms of nonlinear coupled functions. The NCCR model in component form [14,15,23]

$$[\hat{\mathbf{\Pi}} \cdot \nabla \hat{\mathbf{u}}]^{(2)} + \hat{\mathbf{\Pi}}_0 = \hat{\mathbf{\Pi}} q(c\hat{R}),$$
$$\hat{\mathbf{\Pi}} \cdot \hat{\mathbf{Q}}_0 + \hat{\mathbf{Q}}_0 = \hat{\mathbf{Q}} q(c\hat{R}),$$

(2.5)

can be derived as an approximate model suitable for multi-dimensional computations, after applying closure to the high order and dissipation terms in the following exact constitutive equations of the Boltzmann equation [23,28]

$$\rho \frac{d(\mathbf{\Pi}/\rho)}{dt} + \nabla \cdot \left(\langle m\mathbf{ccc}f \rangle - \langle m\text{Tr}(\mathbf{ccc})f \rangle \mathbf{I}/3 \right) + 2[\mathbf{\Pi} \cdot \nabla \mathbf{u}]^{(2)} + 2p[\nabla \mathbf{u}]^{(2)} = \mathbf{\Lambda}^{(\Pi)},$$

$$\rho \frac{d(\mathbf{Q}/\rho)}{dt} + \nabla \cdot \left(\langle mc^2\mathbf{cc}f/2 \rangle - C_p T(p\mathbf{I} + \mathbf{\Pi}) \right) + \langle m\mathbf{ccc}f \rangle : \nabla \mathbf{u} + \frac{d\mathbf{u}}{dt} \cdot \mathbf{\Pi} + \mathbf{Q} \cdot \nabla \mathbf{u}$$
$$+ (p\mathbf{I} + \mathbf{\Pi}) \cdot \nabla C_p T = \mathbf{\Lambda}^{(Q)}.$$

In equations (2.5), $\hat{\mathbf{\Pi}}_0$ and $\hat{\mathbf{Q}}_0$ are determined by the Newtonian law of viscosity and the Fourier law of heat conduction, respectively. The symbols $m, \mathbf{c}, f, \langle \ \rangle, \mathbf{\Lambda}^{(\Pi,Q)}$ denote the mass of gas molecule, the peculiar velocity, the distribution function, the integral in velocity space, and the dissipation terms of shear stress and heat flux, respectively. In addition, the other non-dimensional variables are defined as

$$\hat{\mathbf{\Pi}} \equiv \frac{N_\delta}{p} \mathbf{\Pi}, \ \hat{\mathbf{Q}} \equiv \frac{N_\delta}{p} \frac{\mathbf{Q}}{\sqrt{T/(2\varepsilon)}}, \ \nabla \hat{\mathbf{u}} \equiv -2\eta \frac{N_\delta}{p} \nabla \mathbf{u},$$

$$N_\delta \equiv \frac{\eta_r u_r / L}{p_r} = \text{Kn}M\sqrt{\frac{2\gamma}{\pi}}, \ \varepsilon \equiv \frac{1}{\text{Pr}\,\text{Ec}\,T_r / \Delta T},$$

$$q(c\hat{R}) = \frac{\sinh(c\hat{R})}{c\hat{R}}, \ \hat{R}^2 = \hat{\mathbf{\Pi}} : \hat{\mathbf{\Pi}} + \hat{\mathbf{Q}} \cdot \hat{\mathbf{Q}}.$$

The gas constant c has a value 1.0179 for argon gas molecule [14]. The factor $q(c\hat{R})$ collectively represents the nonlinear nature of transport coefficients associated with the high-order and dissipation terms in the moment equations. The origin and necessity of such nonlinear factor in shock-dominated gas flows was proved recently by Myong [28]. The ultimate source of the high Mach number shock structure singularity arising in moment equations of the Boltzmann equation was shown to be the

unbalanced treatment between two high order kinematic and dissipation terms caused by the overreach of Maxwellian molecule assumption. In compressive gaseous flow, the high order stress-strain coupling term of quadratic nature will grow far faster than the strain term, resulting in an imbalance with the linear dissipation term and eventually a blow-up singularity in high thermal nonequilibrium. Therefore, the nonlinear factor plays an essential role in the well-posedness of constitutive equations in compressive gases. Physically, the nonlinear factor describes the mode of energy dissipation accompanying the irreversible processes. The origin of such factor lies with the consideration of entropy production and the cumulant expansion that provides a resummation procedure for an expansion in the Knudsen number series of the Boltzmann collision integral [23].

It is worthwhile mentioning that a nonlinear factor was already shown to be necessary in the case of general molecules by Grad [29]. The dissipation term, (A5.1) of Grad [29, page 404], can be easily related to the nonlinear factor as follows ($B_1^{(\Pi,Q)}$ being constant)

$$\mathbf{\Lambda}^{(\Pi)} = -\frac{6}{m} B_1^{(\Pi)} \rho \mathbf{\Pi} \left(1 + \frac{\frac{\rho}{m}(B_1^{(Q)} - B_1^{(\Pi)}) \times (\text{quadratic terms})}{-\frac{6}{m}B_1^{(\Pi)}\rho\mathbf{\Pi}} + \text{high order terms} \right).$$

This is equivalent to express the dissipation term with a nonlinear factor F as

$$\mathbf{\Lambda}^{(\Pi)} = -\frac{p}{\eta_{NSF}} \mathbf{\Pi} F(p, T, \mathbf{\Pi}, \mathbf{Q}, \cdots)$$

$$\text{where } F(p, T, \mathbf{\Pi}, \mathbf{Q}, \cdots) = \left(1 + \frac{\frac{\rho}{m}(B_1^{(Q)} - B_1^{(\Pi)}) \times (\text{quadratic terms})}{-\frac{6}{m}B_1^{(\Pi)}\rho\mathbf{\Pi}} + \text{high order terms} \right).$$

A similar nonlinear factor can be also found in the theory developed by Karlin, Dukek and Nonnenmacher [30]. The factor is directly related to the nonlinear viscosity and thermal conductivity in high thermal nonequilibrium states and is also echoed in the well-known Eyring formula in non-Newtonian fluids [31], which describes shear thinning, i.e. the decrease of the viscosity with increasing the velocity gradient (or shear rate).

The non-Newtonian implicit type Eq. (2.5) provides the viscous stress and heat flux, which are essential to define the numerical flux through the cell interfaces. This process becomes trivial in the NSF equations since the viscous stress and heat flux are proportional to the thermodynamic forces. However, owing to the nonlinearity of the constitutive equations, an additional process must be developed for this method. Here, an iterative method will be used to solve the constitutive equations for the given thermodynamic variables (pressure and temperature) and the gradients of velocity and temperature. In the case of a two-dimensional problem, the viscous stress and heat flux components $(\Pi_{xx}, \Pi_{xy}, Q_x)$ on a line in the two-dimensional physical plane induced by thermodynamic forces ($\partial u/\partial x, \partial v/\partial x, \partial T/\partial x$) can be approximated as the sum of two solvers: (1) one on $(\partial u/\partial x, 0, \partial T/\partial x)$, and (2) another on $(0, \partial v/\partial x, 0)$. The first solver is the compression–expansion case and the second is the velocity-shear flow. Both of these solvers can be easily computed within a few iterations [15,16].

3 Validation of the methods

For validating the study of the models, we first considered the DG method for the NSF model, which is the classical approach for macroscale flow simulation. Next, we consider the DG method for the NCCR model, which is proposed for microscale flow simulation. To validate the present methods, we chose two types of shock-vortex interaction as benchmark cases. The first type was the macroscale shock-vortex interaction results of Inoue and Hattori [3] based on the NSF model and the second type was the microscale shock-vortex interaction results of Koffi et al. [11] based on the DSMC.

3.1 Validation of the DG method for the NSF model

In the computational work of Inoue and Hattori [3], shock and Taylor vortex interaction was studied. The conditions of this benchmark case are M_s=1.2(shock Mach number), M_v=0.25, and Re=800. The Reynolds number here is defined by the characteristic size of the core radius of the vortex. Boundary conditions are the fixed upstream boundary conditions in the *x*-axis direction and

are the periodic boundary conditions in the *y*-axis. The sound pressure, defined below, was used to examine the basic structure of vortex deformation:

$$\Delta p = \frac{p - p_s}{p_s},$$
(3.1)

where p is the local pressure and p_s is the pressure after shock wave.

Figs. 2 and 3 show the results of Inoue and Hattori [3] as well as the results of present DG method for the NSF model. The symbol + represents the compression regions, while the symbol –represents the rarefaction regions. The comparison shows that the size, structure and locations of the quadrupolar sound waves, compression regions and rarefaction regions are almost identical. All these features validate the accuracy of the DG method for the NSF model developed in this study.

3.2 Validation of the DG method for the NCCR model

In order to validate the DG method for conservation laws with the NCCR, we select three cases of microscale shock-vortex interaction (see Table 1) investigated by Koffi et al. [11]. Argon gas in its quiescent state surrounding the vortex at an initial temperature of 273K and an initial pressure of 1,013Pa is considered. The core radius varies from 8λ to 12λ.

In Fig. 4 (a), the time evolution of the enstropy, defined as the area integral of the square of the vorticity in the flow field, is compared in order to validate the present NCCR method. These results, including the general trend of the enstropy change with time, were found very close to DSMC results. In order to show another validation result of the NCCR model, a hypersonic gas flow of M=5.48, Kn=0.05 around the cylinder [32] is also considered. Non-dimensional density and temperature distributions at stagnation line in the cylinder gas flow are compared for NCCR, NSF, and DSMC in a previous study [32]. Furthermore, non-dimensional pressure contours are also compared for NCCR, NSF, and DSMC in Fig. 4 (b) for the hypersonic cylinder gas flow of M=5.48, Kn=0.5. Both results show clearly that NCCR performs better than NSF and is very close to DSMC in this high Mach and Knudsen number gas flow. In summary, all these validation studies confirm that all results of the DG method for conservation laws with the NCCR are in qualitative agreement with the DSMC results,

including Koffi et al. [11] in the cases considered. It is clear that the DG NCCR method is effective in both simulations of macroscale and microscale shock-vortex interaction.

4 Microscale shock-vortex interaction

In our simulation, three types of vortexes are chosen for extensive studies. These consist of supersonic vortexes with M_v=1.2, followed by two types of subsonic vortexes with M_v=0.9 and M_v=0.6. In each given vortex Mach number, the core radius increases from 6λ to 16λ with a radius step of 2λ. Consequently, the shock Mach number (M_s) increases from 1.5 to 3.5 with a Mach number step of 0.5. The symbols ○ (3 cases in total) and ★ (90 cases in total) in Fig. 5 represent the DSMC cases of Koffi et al. [11] and this study, respectively. In the definition of the Knudsen number, the core vortex radius (r_1) is considered the characteristic length.

4.1 Vortex deformation through a shock

Four snapshots of the interaction in sound pressure level are shown in Figs. 6-9 for different shock Mach numbers and vortex sizes. The interaction parameters are summarized in Table 2. These four cases are considered representative of the microscale shock-vortex interaction. The former two cases have the same shock Mach number and vortex Mach number (M_s=2.5, M_v=1.2) but different vortex sizes. The vortex core radii for case 1 and case 2 are 8λ and 12λ, respectively. The last two cases have the same shock Mach number and vortex Mach number (M_s=1.5, M_v=1.2) but different vortex sizes. The core radiuses of cases 3 and 4 are also 8λ and 12λ, respectively. Compared with the former two cases, cases 3 and 4 have weaker interactions, resulting from lower shock Mach numbers.

In Fig. 6-9, the positive sound pressure value denotes the compression region, whereas the negative one denotes the rarefaction region. The results show that five regions are generated after the interactions in all four cases. In addition, the former two cases have three strong compression regions, while the last two cases have two weakened compression regions located between two rarefaction regions. Interestingly, quadrupolar acoustic wave source structures, which are typical in the macroscopic shock-vortex interaction, are not observed in any cases. For the comparison, the vortex

core radii at case 2 (M_s=2.5, M_v=1.2, r_1=12λ) were increased to near macroscale. It was found from Figs. 10 and 11 of the time evolution of sound pressure after the shock wave crossing the center of the vortex that quadrupolar acoustic structures reemerge when the vortex core radii exceed 112λ. According to the linearized theory of Ribner [33], which predicts the quadrupolar acoustic wave in the macroscale shock-vortex interaction, the pressure jump varies around the vortex and generates a quadrupole field. The interaction also causes a $1/r$ potential flow around the vortex core and the pressure of this potential flow field can be expressed as

$$p \sim \frac{v_{\max}}{V} \left(\frac{r_1}{at} \right)^{1/2}.$$

Here, a is the speed of sound at upstream of shock, t is the time, r_1 is the radius of the vortex core, v_{max} is the peak velocity in the vortex field at upstream of the shock, and V is the upstream velocity of the shock. As obvious in the equation, the pressure jump is weakened in the microscale shock-vortex interaction where the radius of the vortex core r_1 is very small, which results in the disappearance of the quadrupolar acoustic wave.

The results of the generation of compression regions in the interaction conform that the physical phenomena are in general different for the weak and strong interactions. To better understand the nature of interaction, we introduce the vorticity as defined below

$$\Omega_z = \frac{\partial V_y}{\partial x} - \frac{\partial V_x}{\partial y}.$$

Cases 1 and 3 have the same initial vorticity (M_v=1.2 and r_1=8λ) but differ in shock Mach numbers (M_s=2.5 for case 1 and M_s=1.5 for case 3). The vorticity distribution differs remarkably after interaction, as shown in Figs. 12 and 14 of vorticity contours when the vortex passes a shock wave. For case 1, which has a high shock Mach number, a large regime of negative vorticity is observed. The composite vortex used here has a negative vorticity in its core and a positive vorticity in the outside ring; thus, the decreasing vorticity value in the core indicates a non-negligible vorticity generation. As shown in Figs. 13 and 15, this phenomenon is also evident in the comparison between

cases 2 and 4, which have the same initial vorticity (M_v=1.2 and r_1=12λ) but different shock Mach numbers (M_s=2.5 for case 2 and M_s=1.5 for case 4).

Numerical experiments for different shock-vortex interactions show that the flow structure may differ notably for different shock Mach numbers or vortex sizes at the microscale. The vortex deformation through a shock wave, in particular, seems to be strongly dependent on the interaction strength. Thus, the quantitative results of vorticity change during the interaction may be obtained by investigating the overall dynamics of net production and the dissipation of vorticity.

4.2 Overall dynamics through a shock wave

As shown in Fig. 4(a), a substantial attenuation of enstrophy with time is also observed in the validation cases. These results are in stark contrast with those of the macroscale interaction that shows an increase in enstrophy when the vortex crosses a shock wave [22]. In addition, different interaction parameters cause different vortex deformations as demonstrated in the previous section. Quantitative studies of these features can be performed by investigating the area-weighted vortex dynamics.

4.2.1 Enstrophy and dissipation rate

The mechanisms leading to the generation or attenuation of vorticity in the interaction can be investigated by considering the time evolution of the enstrophy [11], which is defined as

$$\text{Enstrophy } (t) = \int_A \Omega_z^2(x, y, t)dxdy. \tag{4.1}$$

The viscous effect is investigated by introducing the area-weighted dissipation rate of the kinetic energy

$$\text{Dissipation rate } (t) = \int_A E(x, y, t)dxdy. \tag{4.2}$$

Here $E(x, y, t)$ represents the dissipation rate per unit volume and is defined as

$$E(x, y, t) = -(\Pi_{xx} S_{xx} + \Pi_{xy} S_{xy} + \Pi_{yx} S_{yx} + \Pi_{yy} S_{yy}), \tag{4.3}$$

where

$$S_{ij} = \frac{\partial V_i}{\partial x_j}.$$

The time evolutions of enstrophy and the dissipation rate are plotted in Figs. 16 and 17 for the four different cases. The shock wave begins to interact with the vortex around 200 ns and ends around 600 ns. The trends are quite different for the first two (cases 1 and 2 with higher shock Mach numbers) cases and the last two cases (cases 3 and 4 with lower shock Mach numbers). An increase in enstrophy is observed in cases 1 and 2 during the interaction process (200-600 ns). On the other hand, a decrease of enstrophy is found in cases 3 and 4 throughout the entire interaction process. The difference is also evident in the time evolution of the dissipation rate illustrated in Fig. 17. The dissipation rates of the first two cases are much greater than those of the last two cases. In addition, there is an increase in the dissipation rate in cases 1 and 2 during the interaction process. On the other hand, the dissipation rates in cases 3 and 4 appear to remain constant over time during the entire interaction process. The reason may be that the viscous stress and its change due to high Knudsen numbers dominate the flow structure during the interaction and cause the generation (increase) or attenuation (decrease) of the overall dynamics (enstrophy and dissipation rate) [34]. Weak interactions with low shock Mach number or small vortex size result in weak viscous effects and then cause low dissipation rate. This is one of the major characteristics that are found in microscale shock-vortex interactions.

Numerical experiments on enstrophy and the dissipation rate show that the overall dynamics differs considerably for strong and weak interactions. We therefore conduct a detailed study of vorticity transportation in order to gain a deeper understanding of the nature of interaction.

4.2.2. Vorticity transportation

The following relation can be derived in a straightforward approach in the two-dimensional case [11,35].

$$\frac{D\Omega_z}{Dt} = -\Omega_z \left(\frac{\partial V_x}{\partial x} + \frac{\partial V_y}{\partial y} \right) + \frac{1}{\rho^2} \left(\frac{\partial \rho}{\partial x} \frac{\partial p}{\partial y} - \frac{\partial \rho}{\partial y} \frac{\partial p}{\partial x} \right)$$
$$+ \left[\frac{\partial}{\partial y} \left(\frac{1}{\rho} \frac{\partial \Pi_{xx}}{\partial x} + \frac{1}{\rho} \frac{\partial \Pi_{xy}}{\partial y} \right) - \frac{\partial}{\partial x} \left(\frac{1}{\rho} \frac{\partial \Pi_{yx}}{\partial x} + \frac{1}{\rho} \frac{\partial \Pi_{yy}}{\partial y} \right) \right].$$

(4.4)

Equation (4.4) describes three dynamically significant processes for the vorticity component Ω_z, namely, vorticity generation through the dilatation strain rate, baroclinic generation through the interaction of pressure and density gradients, and viscous vorticity generation through the viscous effects.

The net area-weighted vorticity generation is defined as

$$\text{Net vorticity } (x, y, t) = \int_A \frac{D\Omega_z}{Dt} dxdy.$$

(4.5)

The net area-weighted dilatational vorticity generation is computed as follows:

$$\text{Dilatational vorticity } (x, y, t) = -\int_A \Omega_z \left(\frac{\partial V_x}{\partial x} + \frac{\partial V_y}{\partial y} \right) dxdy.$$

(4.6)

The net area-weighted baroclinic vorticity generation is given by

$$\text{Baroclinic vorticity } (x, y, t) = \int_A \frac{1}{\rho^2} \left(\frac{\partial \rho}{\partial x} \frac{\partial p}{\partial y} - \frac{\partial \rho}{\partial y} \frac{\partial p}{\partial x} \right) dxdy.$$

(4.7)

The net area-weighted viscous vorticity generation is expressed as

$$\text{Viscous vorticity } (x, y, t) = \int_A \left[\frac{\partial}{\partial y} \left(\frac{1}{\rho} \frac{\partial \Pi_{xx}}{\partial x} + \frac{1}{\rho} \frac{\partial \Pi_{xy}}{\partial y} \right) - \frac{\partial}{\partial x} \left(\frac{1}{\rho} \frac{\partial \Pi_{yx}}{\partial x} + \frac{1}{\rho} \frac{\partial \Pi_{yy}}{\partial y} \right) \right] dxdy. \quad (4.8)$$

The time evolutions of the four different types of net vorticity transportation are plotted in Figs. 18-21 for cases 1-4, which show that the net viscous vorticity generation is the most dominant mechanism, followed by net dilatational vorticity and baroclinic vorticity generations. Net vorticity changes through dilatational generation, baroclinic generation, and viscous generation are significant in the interaction process, in particular, for cases 1-2. For strong interactions with high shock Mach numbers, the viscous effects play a dominant role in the interaction (see Fig. 21), resulting in

significant increase in the dissipation rate (see Fig. 19). Thus, a large change in net area-weighted vorticity generation is observed for strong interactions (see Fig. 20).

4.3 Summary of microscale shock-vortex interaction

Unique physical phenomena, which may differ from the macroscale shocks-vortex interaction, can occur in the microscale shock-vortex interaction. For example, three compression regions and two rarefaction regions can be formed after the interaction at microscale. The strengths of these compression and rarefaction regions greatly depend on the interaction parameters, which are determined by the shock and vortex Mach numbers. Furthermore, net viscous vorticity generation is the most dominant factor in the net vorticity transportation processes, followed by dilatational vorticity generation and baroclinic vorticity generation. For strong interactions with high shock or vortex Mach numbers, viscous vorticity causes a significant increase in the dissipation rate during the interaction, which results in an increase in enstrophy. Although the increase in enstrophy for strong interaction at the microscale is similar to that at the macroscale, quadrupolar acoustic wave structure is not observed in any cases. For weak interactions with low shock or vortex Mach numbers, although the viscous effects are also dominant, viscous vorticity generation and dilatational vorticity generation occur at lower levels. Viscous effects also cause a small increase in the dissipation rate during the interaction, which results in the decrease in enstrophy throughout the entire process for weak interactions.

5 The effects of interaction parameters on the microscale shock-vortex interaction

In order to explain the effects of interaction parameters on the microscale shock-vortex interaction, a diagram which is observed in the present study is plotted in Fig. 22. The composite vortex, which rotates clockwise, is fixed, and the planar shock passes through from left to right. For convenience, we divide the composite vortex into four regions, similar to the quadrant division method in a Cartesian coordinate system. The plot of the velocity distribution curve in the vortex along the radius

is also shown in Fig. 22. The pressure distribution curve in the inner region of the vortex affected by the size and vortex Mach number is shown in Fig. 23. The pressure distribution curve along the radius appears in the *s*-curve, and the maximum pressure gradient appears at the core radius of the composite vortex r_1.

Typical sound pressure structures observed in the present study are shown in Fig. 23. Because of clockwise velocity of the vortex, the shock becomes *S*-shaped after passing through the composite vortex. In addition, while the direction of the velocity of the bottom half is the same as that of the local flow velocity, the direction of the velocity of the upper half of the vortex is opposite to that of the local flow velocity in the *x*-axis direction, causing the deformation of the vortex and generation of five elliptical regions. Regions 1, 2, and 5 are compressive regions, whereas regions 3 and 4 are rarefaction regions.

5.1 Effect of the shock Mach number

We selected three cases to demonstrate the effects of the shock Mach number: M_s=1.5, 2.5, 3.5, with the same vortex Mach number M_v=1.2, vortex radius r_1=12 λ. As shown in Figs. 7, 9, and 24, the high shock Mach number causes stronger shock-vortex interaction. Besides, the high shock Mach number blocks the diffusion of the expansion wave caused by the vortex. Consequently, the high shock Mach number diminishes the vortex region and reduces rarefaction region 4 and strengths compressive regions 1 and 2. Furthermore, the high shock Mach number yields a tendency for region 1 to break the siege boundary formed by the vortex.

The overall dynamics also become different for different shock Mach numbers, as shown in Figs. 25 and 26. With an increasing shock Mach number, the increase in the dissipation rate during the interaction is enhanced. For example, the increase is 200 Pa.m^2/s for M_s=3.5, while it is reduced to 6 Pa.m^2/s for M_s=1.5. Furthermore, during the interaction, an enstrophy increase is observed in cases 2 (M_s=2.5, M_v=1.2) and 5 (M_s=3.5 M_v=1.2), whereas an enstrophy decrease is observed in case 4 (M_s=1.5, M_v=1.2).

5.2. Effect of the vortex size

As shown in Figs. 6, 7 and 27, we selected three cases to demonstrate the effect of the vortex size: r_1 =8λ, 12λ, 16λ, with the same shock Mach number M_s=2.5, vortex Mach number M_v=1.2. As the size of the vortex decreases, the pressure gradient at the core radius of the vortex increases significantly, and the unstable effect of gas in this zone becomes strong (see Fig. 23). Consequently, the extrusion of compressive region 2 to the inner of vortex is strengthened. At a certain degree of extrusion strength, compressive regions 2 and 5 become connected, while rarefaction regions 3 and 4 become two independent islands. The results confirm that the overall dynamics differ for different vortex sizes (see Figs. 28 and 29). With a decreasing vortex size, the increase in the dissipation rate during the interaction is weakened. For example, the increase is 40 Pa.m^2/s for r_1=16λ, while it is reduced to15 Pa.m^2/s for r_1=8λ. Furthermore, the enstrophy increase is reduced with decreasing vortex size. Therefore, in case 1 involving the smaller vortex size r_1=8λ, a very small enstrophy increase is observed, while large enstrophy increases are found in cases 2 (r_1=12 λ) and 6(r_1=16λ).

5.3. Effect of the vortex Mach number

We selected three cases to explain the effect of the vortex Mach number: M_v=1.2, 0.9, 0.6, with the same shock Mach number M_s=2.5, vortex radius size r_1=12λ. As shown in Figs. 7, 30, and 31, the decreasing vortex Mach number weakens the shock-vortex interaction and the expanding vortex. It in turn causes a reduction in the size of compressive regions 1 and 2. In case of the overall dynamics (enstrophy and dissipation rate) shown in Figs. 32 and 33, the results show that, with a decreasing vortex Mach number, the increase of the dissipation rate during the interaction is weakened. For example, the increase is 39 Pa.m^2/s for M_v=1.2, while it is reduced to5 Pa.m^2/s for M_v=0.6. Moreover, the enstrophy increase is reduced with the decreasing vortex Mach number. During the interaction, considerable enstrophy increases are observed in cases 2 (M_s=2.5, M_v=1.2) and 7 (M_s=2.5, M_v=0.9), whereas a very small enstrophy increase is observed in case 8 (M_s=2.5, M_v=0.6).

5.4 Summary of the effects of interaction parameters

The analysis demonstrates that vortex deformation in the microscale shock-vortex interaction is closely related to the vortex size and interaction parameters of the shock and vortex Mach numbers. During the interaction, the significant increase of the viscous dissipation rate can lead to an enstrophy increase (net vorticity generation), whereas different shock-vortex interaction parameters lead to different increases in the viscous dissipation rate. The study of the effects of interaction parameters confirms that the shock Mach number, vortex Mach number and vortex size determine the interaction strength and the associated change of dissipation rate during the interaction. For example, the enstrophy increase or decrease depends on these parameters; in general, it increases with increasing shock and vortex Mach numbers and the vortex size. Further, there exists the momentary rise in the evolution of enstrophy in such cases.

6 Conclusions and remarks

Extensive computational investigation on the basis of the conservation laws with non-Newtonian implicit type nonlinear coupled constitutive relations is reported to better understand the physics of microscale shock-vortex interaction of argon gas in thermal nonequilibrium. To validate the present mixed DG method, the macroscale shock-vortex interaction problem studied through a high-order NSF numerical method is first solved to validate the DG method of the NSF model. The present method is shown to reproduce all flow features identified in previous works, including the size, structure, and locations of the sound waves of the compression and rarefaction regions. Then, the microscale shock-vortex interaction problem studied through the DSMC method is considered to validate the present DG method of the NCCR model. All cases demonstrate that the main features identified in their work, including the enstrophy behavior, are also found in the present simulation.

The present simulation method successfully characterizes a large number of flow cases of the interactions of a planar shock up to Mach 3.5 with a transverse composite micro vortex on the shock thickness scale. Through computational simulation, new physical features are found in the microscale shock-vortex interaction. For example, the quadrupolar acoustic wave structure, which is the major feature at the macroscale, is not observed. Our study also reveals that three compression regions and

two rarefaction regions are formed after interaction, irrespective of the interaction parameters. The strength of these compression and rarefaction regions greatly depends on the interaction parameters determined mainly by the shock and vortex Mach numbers. Furthermore, we found that the net viscous vorticity generation is the most dominant mechanism, followed by dilatational vorticity and baroclinic vorticity generations.

Moreover, we found that the strong shock-vortex interaction in high shock or vortex Mach numbers can cause an increase in enstrophy. For strong interactions with high shock or vortex Mach numbers, net viscous vorticity generation causes significant increases in the dissipation rate during the interaction, which results in an increase in enstrophy during the interaction. For weak interactions with low shock or vortex Mach numbers, although viscous effects are dominant, viscous vorticity generation and dilatational vorticity generation are at low levels, which causes negligible changes in the dissipation rate during the interaction and the decrease in enstrophy throughout the entire process.

Additionally, the effects of the shock Mach number, vortex Mach number, and vortex size on the microscale shock vortex interaction are explored in detail. The shock Mach number, vortex Mach number and vortex size turn out to play a critical role in the physical model of the deformation of the vortex and the strength of interaction. In addition, these interaction parameters are shown to govern the net viscous vorticity generation, the change of dissipation rate and the increase or decrease in enstrophy during the interaction.

The present study has been limited to the investigation of monatomic argon gas for computational simplicity. It is well known, however, that the rotational modes of a diatomic molecule, in particular the bulk viscosity, play a non-negligible role in the nonequilibrium gases. Extension of the present line of investigation to the study of the microscale shock-vortex interaction in diatomic gases will be the subject of future work.

Acknowledgments

References

[1] Ellzey JL, Henneke MR, Picone JM, Oran ES. The interaction of a shock with a vortex: shock distortion and the production of acoustic waves. Phys Fluids 1995;7:172-184.

[2] Erlebacher G, Hussaini MY. Interaction of a shock with a longitudinal vortex. J Fluid Mech 1997; 337:129-153.

[3] Inoue O, Hattori Y. Sound generation by a two-dimensional circular cylinder in a uniform flow. J Fluid Mech 1999; 380:81-116.

[4] Inoue O, Hattori Y, Sasaki T. Sound generation by coaxial collision of two vortex rings. J Fluid Mech 2000;424:327-365.

[5] Inoue O, Hatakeyama N. Sound generation by shock vortex interactions. J Fluid Mech 2002;471:285-314.

[6] Liang SM, Tai CS. Analysis and prediction of shock-induced near-field acoustics from an exhaust pipe. Comput. Fluids 2011;45(1):222-232.

[7] Zhang SH, Zhang YT, Shu CW. Multistage interaction of a shockwave and a strong vortex. Phys Fluids 2005;17:116101.

[8] Chatterjee A, Vijayaraj S. Multiple sound generation in interaction of shock wave with strong vortex. AIAA J 2008;46:2558-2567.

[9] Chang KS, Barik H, Chang, SM. The shock-vortex interaction patterns affected by vortex flow regime and vortex models. Shock Waves 2009;19:349-360.

[10] Koffi K, Njante JP, Watkins CB, Andreopoulos, Y. Microscale shock interaction with shock-thickness scale vortex using direct simulation Monte Carlo. AIAA Paper 2005-4898.

[11] Koffi K, Andreopoulos Y, Watkins, CB. Dynamics of microscale shock/vortex interaction. Phys Fluids 2008; 20:126102.

[12] Bird GA. Molecular gas dynamics and the direct simulation of gas flows. Oxford Clarendon Press; 1994.

[13] Prasanth PS, Kakkassery JK. Direct simulation Monte Carlo (DSMC): A numerical method for transition-regime flows-a review. J Indian Inst Sci 2006; 86:169-192.

[14] Myong RS. Thermodynamically consistent hydrodynamic computational models for high-Knudsen-number gas flows. Phys Fluids 1999;11:2788-2802.

[15] Myong RS. A computational method for Eu's generalized hydrodynamic equations of rarefied and microscale gas dynamics. J Comput Phys 2001;168:47-72.

[16] Myong RS. A generalized hydrodynamic computational model for rarefied and microscale diatomic gas flows. J Comput Phys 2004;195:655-676.

[17] Ahn JW, Kim C. An axisymmetric computational model of generalized hydrodynamic theory for rarefied multi-species gas flows. J Comput Phys 2009;228:4088-4117.

[18] Mcphail YM. An experimental rocket model and numerical plume boundary studies for under-expanded flow. Ph.D. Thesis. The University of New South Wales; 2011.

[19] Myong RS. A full analytical solution for the force-driven compressible Poiseuille gas flow based on a nonlinear coupled constitutive relation. Phys Fluids 2011;23:012002.

[20] Rawat PS, Zhong XL. On high-order shock-fitting and front-tracking schemes for numerical simulation of shock-disturbance interactions. J Sci Comput 2010;229:6744-6780.

[21] Prakash A, Parsons N, Wang X, Zhong X. High-order shock-fitting methods for direct numerical simulation of hypersonic flow with chemical and thermal nonequilibrium. J Comput Phys 2011;230:8474-8507.

[22] Rault A, Chiavassa G, Donat R. Shock-vortex interactions at high Mach numbers. J Sci Comput 2003;19:347-371.

[23] Eu BC. Kinetic theory and irreversible thermodynamics. Wiley; 1992.

[24] Bassi F, Rebay S. A high-order accurate discontinuous finite element method for the numerical solution of the compressible Navier-Stokes equations. J Comput Phys 1997;131:267-279.

[25] Li BQ. Discontinuous finite elements in fluid dynamics and heat transfer. Springer-Verlag; 2006.

[26] Krivodonova L. Limiters for high-order discontinuous Galerkin methods. J Comput Phys 2007;226:879-896.

[27] Cockburn B, Shu CW. Runge-Kutta discontinuous Galerkin methods for convection dominated problems. J Sci Comput 2001;16:173-261.

[28] Myong RS. On the high Mach number shock structure singularity caused by overreach of Maxwellian molecules. Phys Fluids 2014;26:056102.

[29] Grad H. On the kinetic theory of rarefied gases. Comm Pure Appl Math 1949;2:331-407.

[30] Karlin IV, Dukek G, Nonnenmacher TF. Invariance principle for extension of hydrodynamics: nonlinear viscosity. Phys Rev E 1997;55:1573-1576.

[31] Jou D, Vazquez JC, Lebon G. Extended irreversible thermodynamics, Springer; 2006.

[32] Le NTP, Xiao H, Myong RS. A triangular discontinuous Galerkin method for non-Newtonian implicit constitutive models of rarefied and microscale gases. J Comput Phys 2014; 273:160-184.

[33] Ribner HS. Cylindrical sound wave generated by shock-vortex interaction. AIAA J 1985;23:1708-1715.

[34] Andreopoulos Y, Agui JH, Briassulis G. Shock wave turbulence interactions. Ann Rev Fluid Mech 2000;32:309-345.

[35] Kevlahan NKR. The vorticity jump across a shock in a non-uniform flow. J Fluid Mech 1997;341:371-384.

Case	r_1	M_s	M_v	λ (Pre-shock, m)	λ (Post-shock, m)
1	8λ	2	1.2	6.26×10^{-6}	2.72×10^{-6}
2	12λ	2	1.2	6.26×10^{-6}	2.72×10^{-6}
3	10λ	3	1.2	6.26×10^{-6}	2.72×10^{-6}

Table I. Benchmark cases for validation of the NCCR model.

Case	r_1	M_s	M_v
1	8λ	2.5	1.2
2	12λ	2.5	1.2
3	8λ	1.5	1.2
4	12λ	1.5	1.2

Table II. Cases of vortex deformation through a shock.
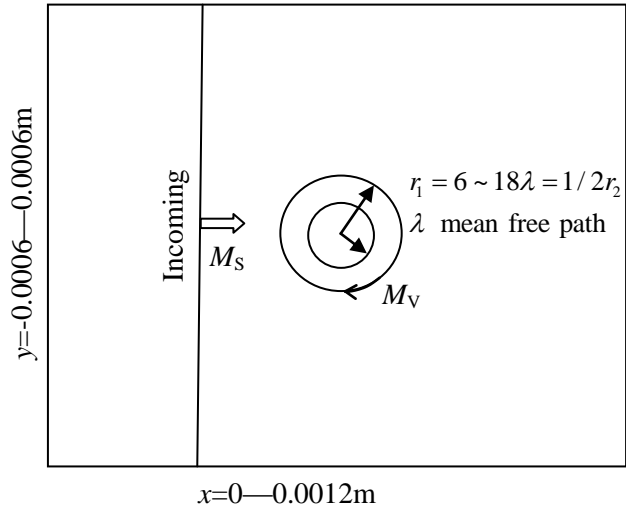
Fig. 1. Physical system of microscale shock-vortex interaction.
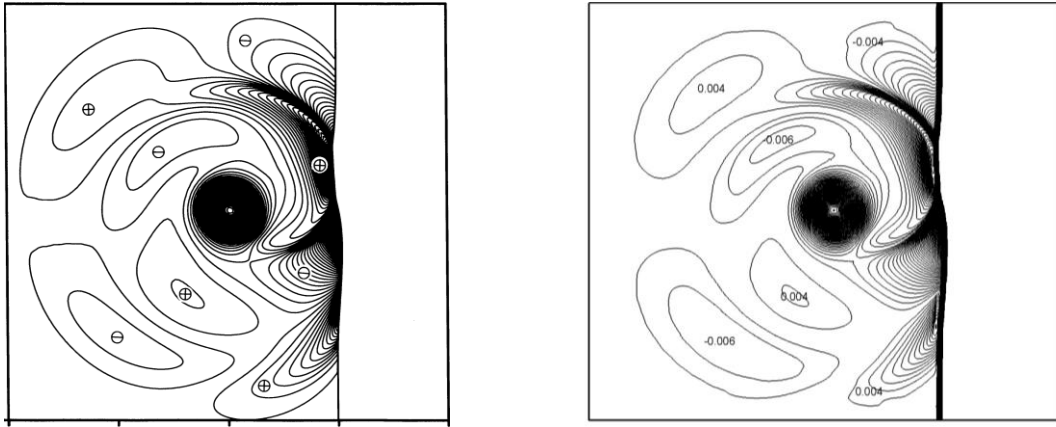
Fig. 2. Sound pressure field in Inoue's result [3]. **Fig. 3.** Sound pressure field in the present result.
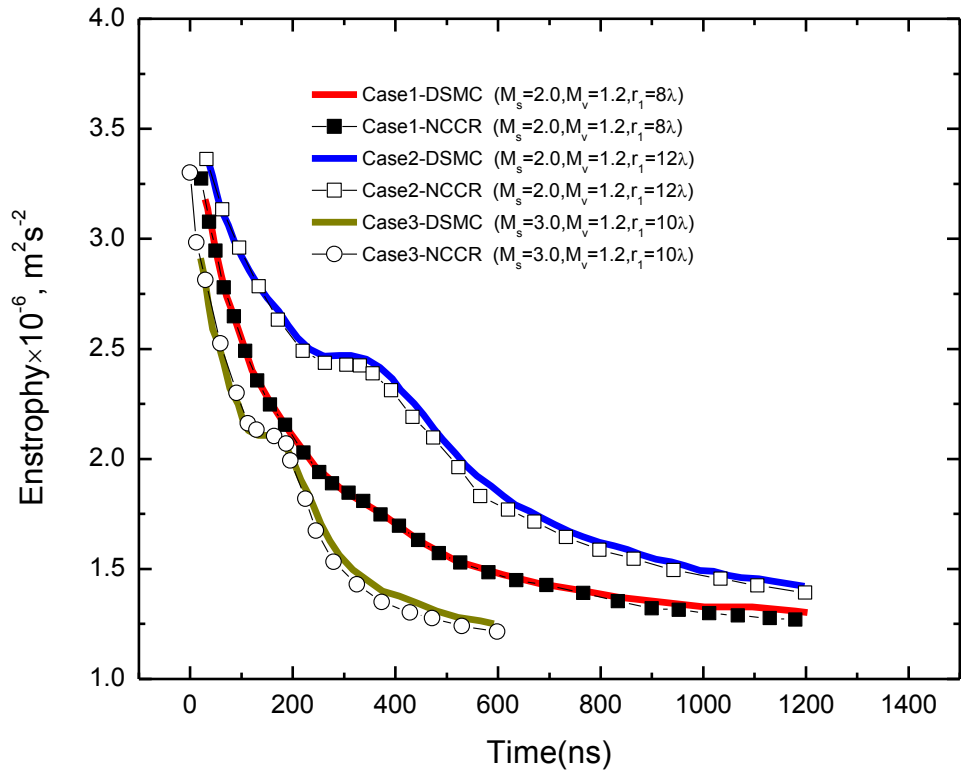
Fig. 4(a). NCCR validation in micro shock vortex interaction ([11]; time evolution of area-weighted enstrophy).
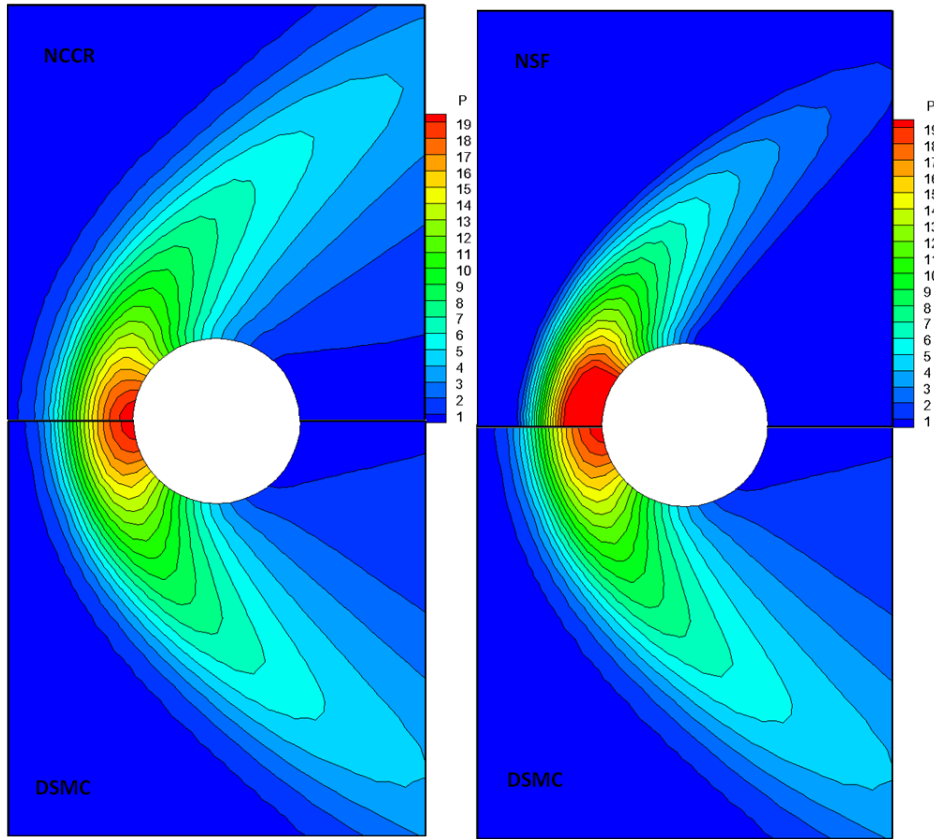
Fig. 4(b). NCCR validation in hypersonic cylinder flow (non-dimensional pressure contours; argon gas; $M = 5.48$ and Kn = 0.5): left –NCCR with the nonlinear factor and DSMC; right – NSF and DSMC.
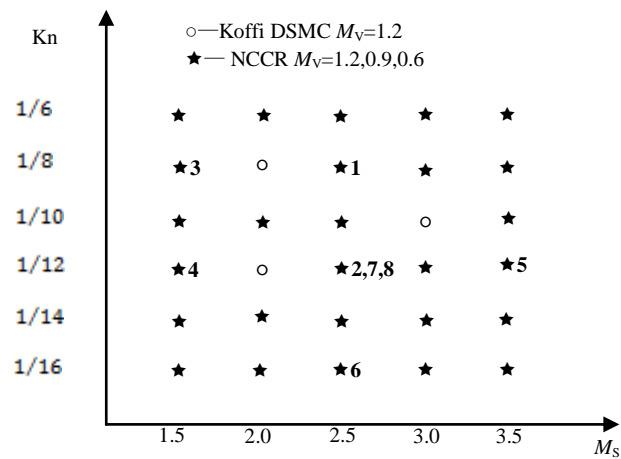
Fig. 5. Simulation cases of the present study and Koffi et al. [11] study.
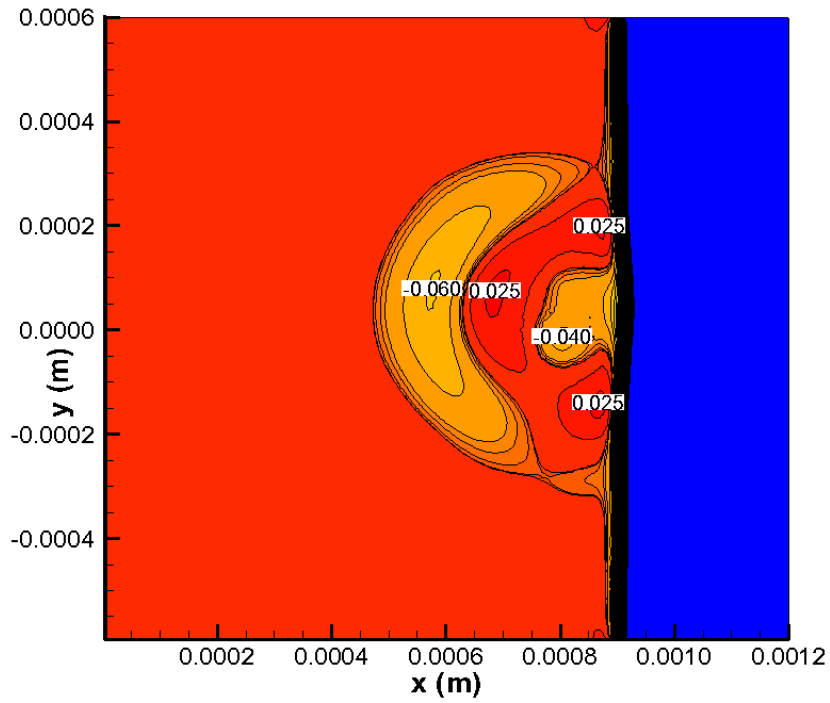
*M*ₛ=2.5, *M*ᵥ=1.2, *r*₁=8λ, Kn=0.125, *t*=715 ns

Fig. 6. Sound pressure contour for case 1.
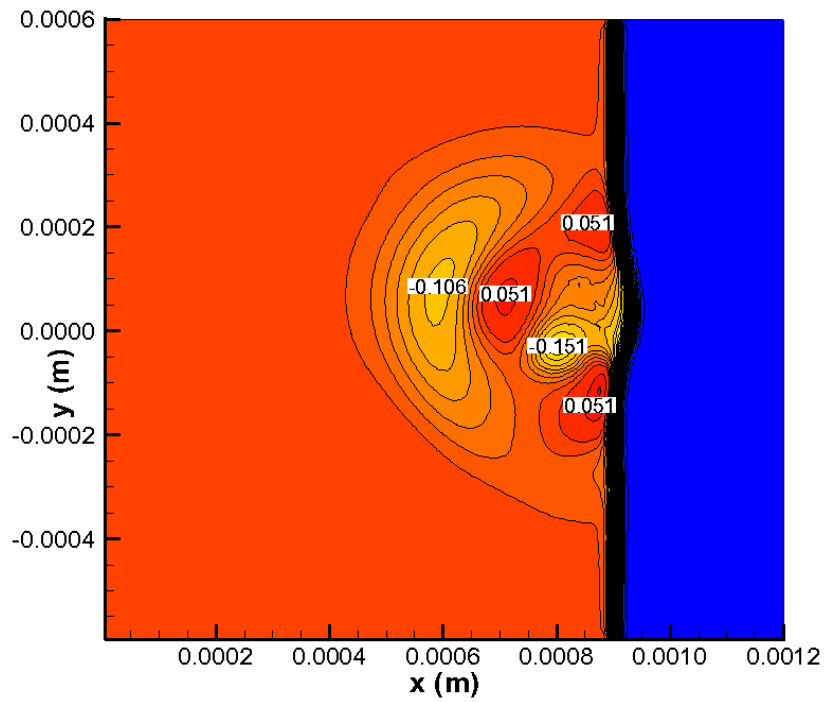
*M*ₛ=2.5, *M*ᵥ=1.2, *r*₁=12λ, Kn=0.083, *t*=715 ns

Fig. 7. Sound pressure contour for case 2.
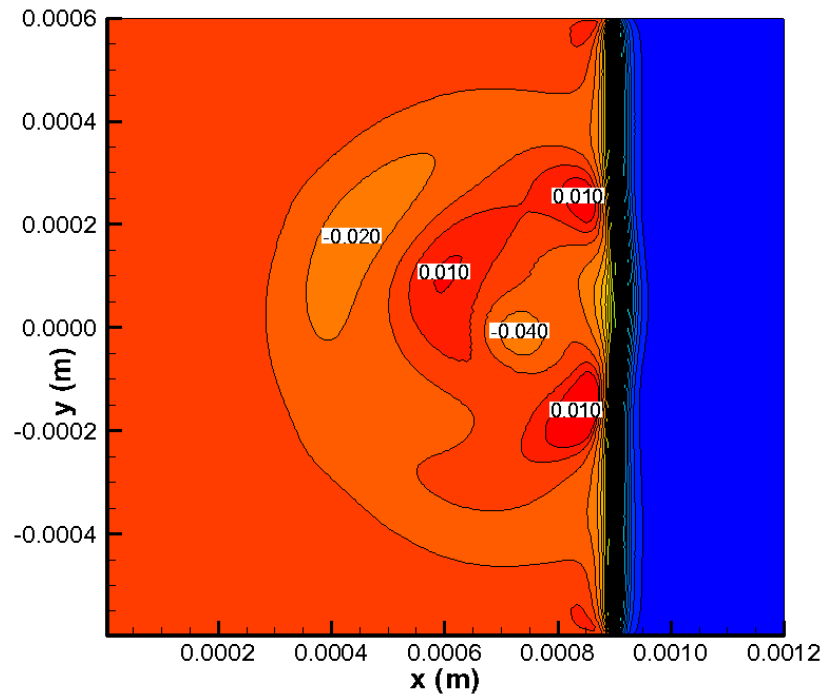
M_s=1.5, M_v=1.2, r_1=8λ, Kn=0.125, t=1,194 ns

Fig. 8. Sound pressure contour for case 3.
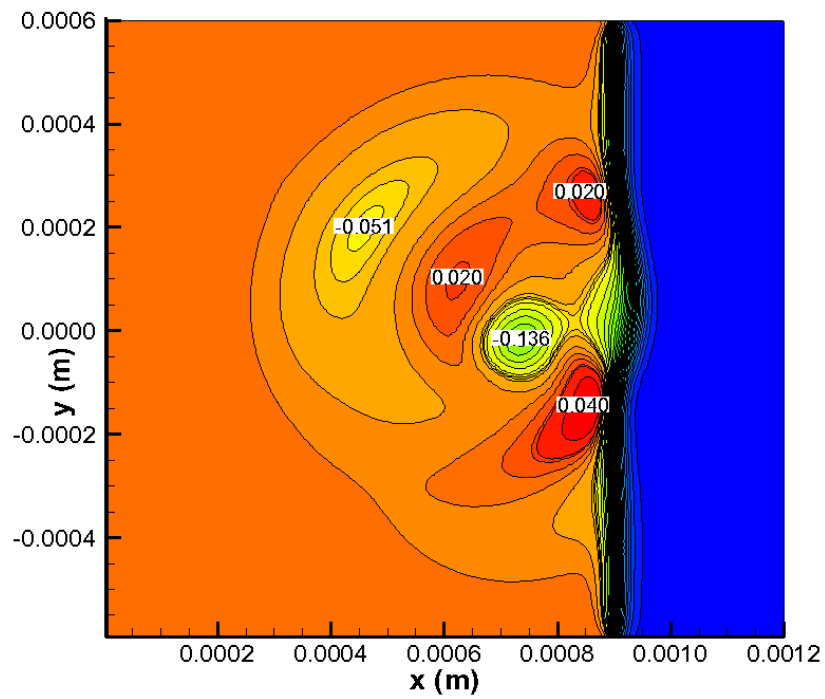
M_s=1.5, M_v=1.2, r_1=12λ, Kn=0.083, t=1,194 ns

Fig. 9. Sound pressure contour for case 4.
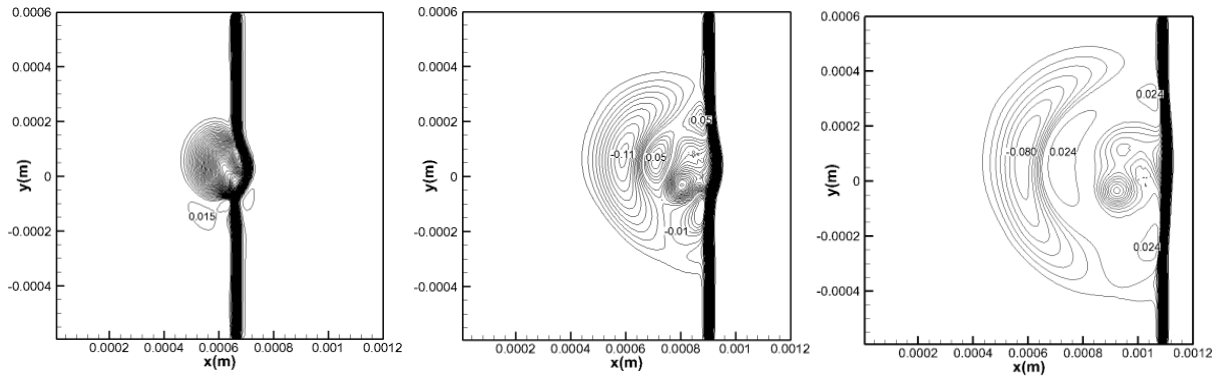
Fig.10. Time evolution of sound pressure for the case of $M_s=2.5$, $M_v=1.2$, $r_1=12\lambda$.
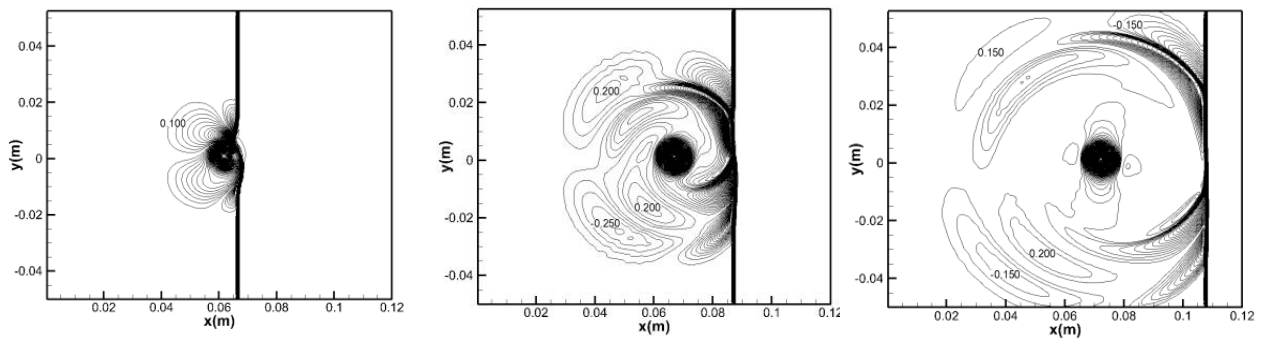
Fig.11. Time evolution of sound pressure for the case of $M_s=2.5$, $M_v=1.2$, $r_1=112\lambda$.
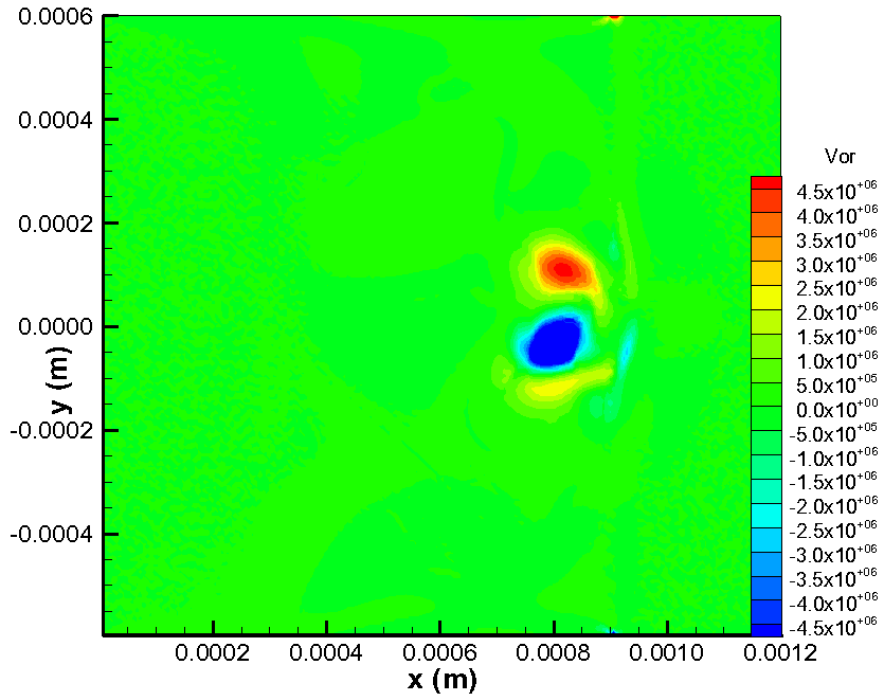
M_s=2.5, M_v=1.2, r_1=8λ, Kn=0.125, t=715 ns

Fig. 12. Vorticity contour for case 1.
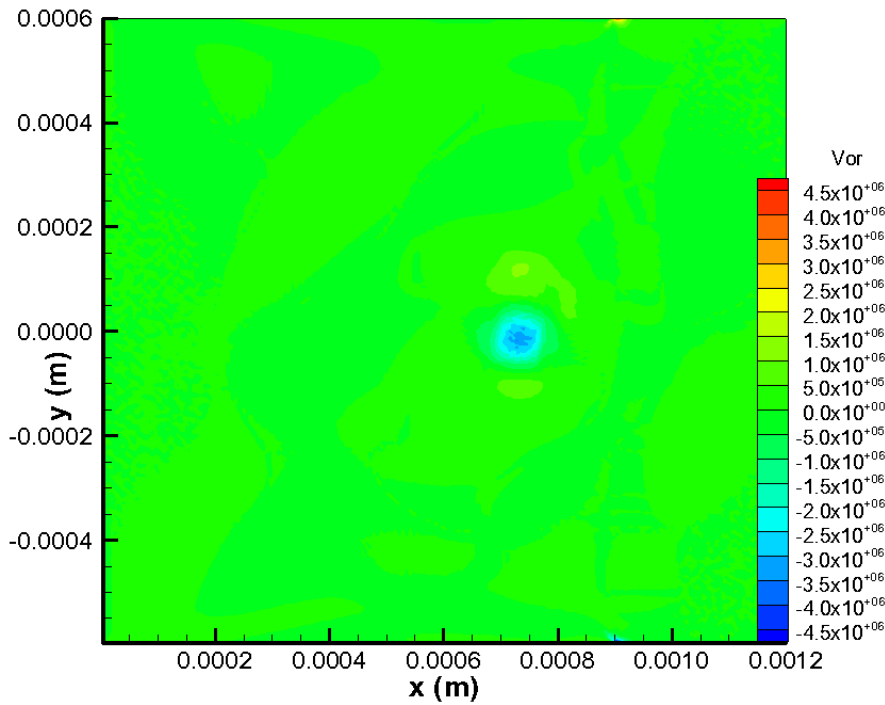
M_s=2.5, M_v=1.2, r_1=12λ, Kn=0.083, t=715 ns

Fig. 13. Vorticity contour for case 2.
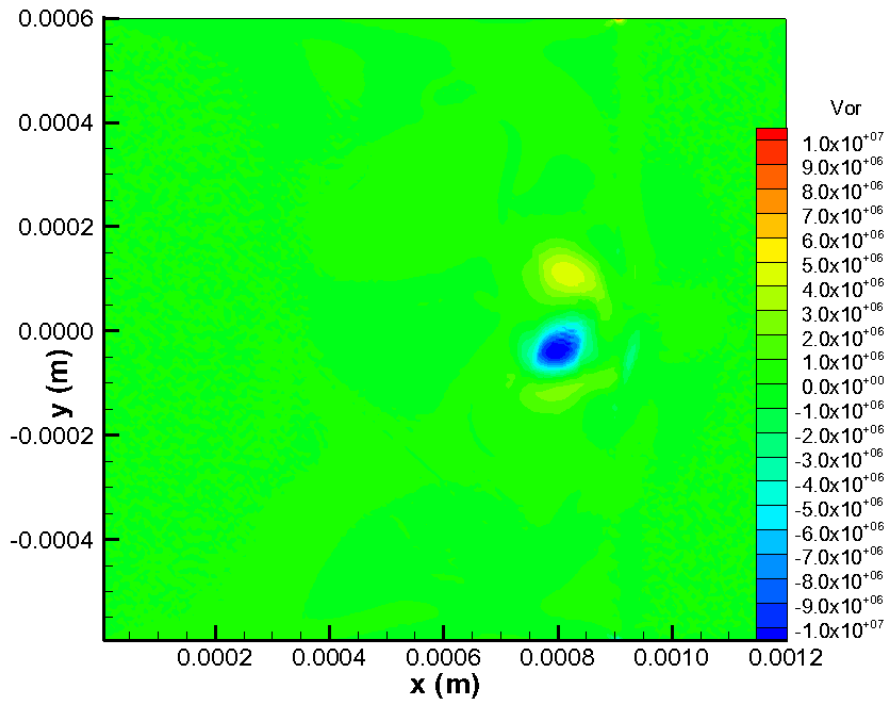
M_s=1.5, M_v=1.2, r_1=8λ, Kn=0.125, t=1,194 ns

Fig. 14. Vorticity contour for case 4.
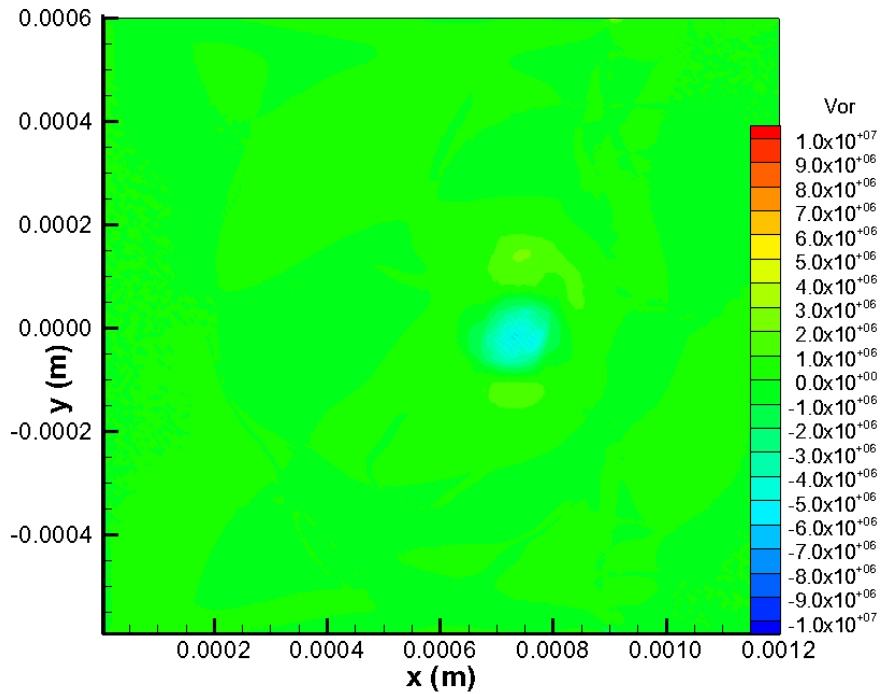
M_s=1.5, M_v=1.2, r_1=12λ, Kn=0.083, t=1,194 ns

Fig. 15. Vorticity contour for case 4.
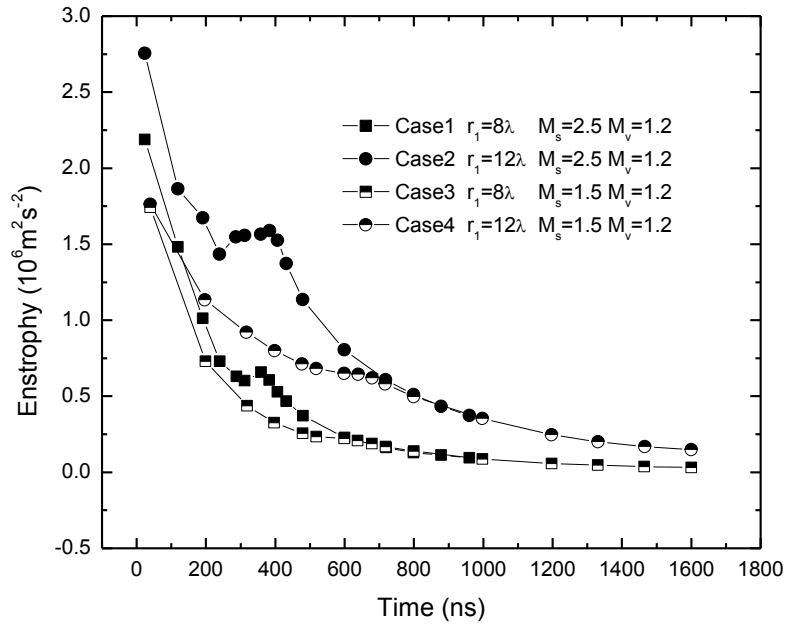
Fig. 16. Time evolution of enstrophy (cases 1-4).
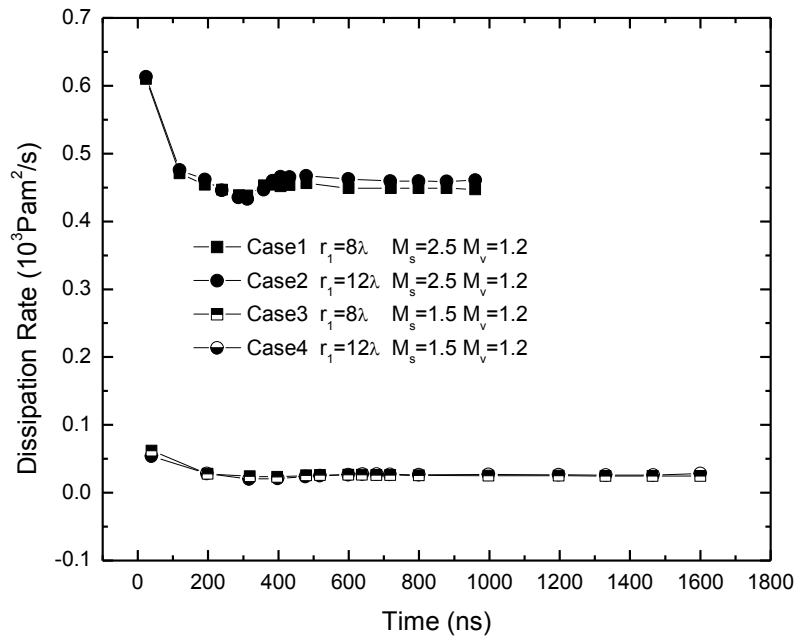
Fig. 17. Time evolution of dissipation rate (cases 1-4).
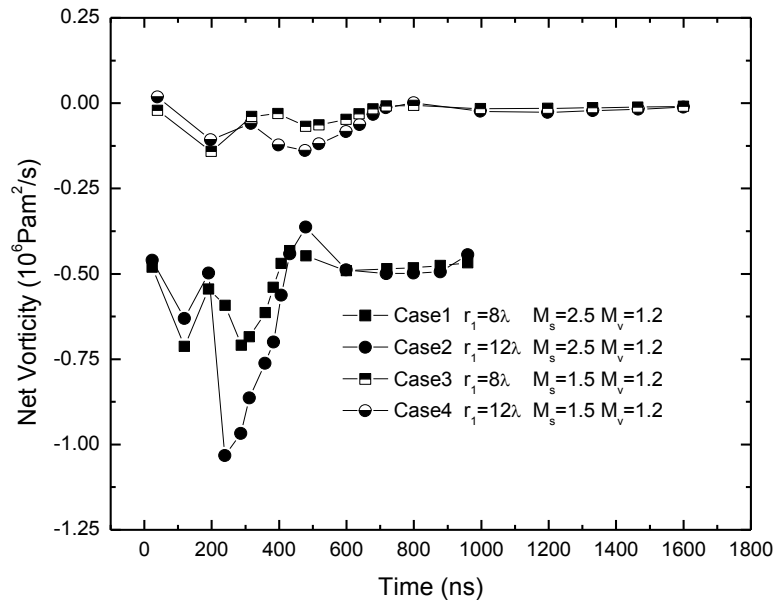
Fig. 18. Time evolution of net vorticity (cases 1-4).
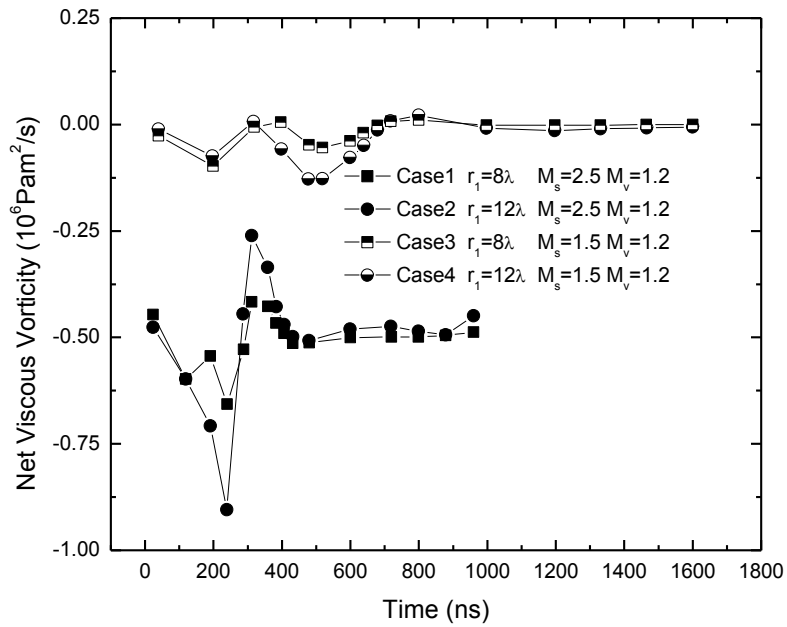
Fig. 19. Time evolution of net viscous vorticity (cases 1-4).
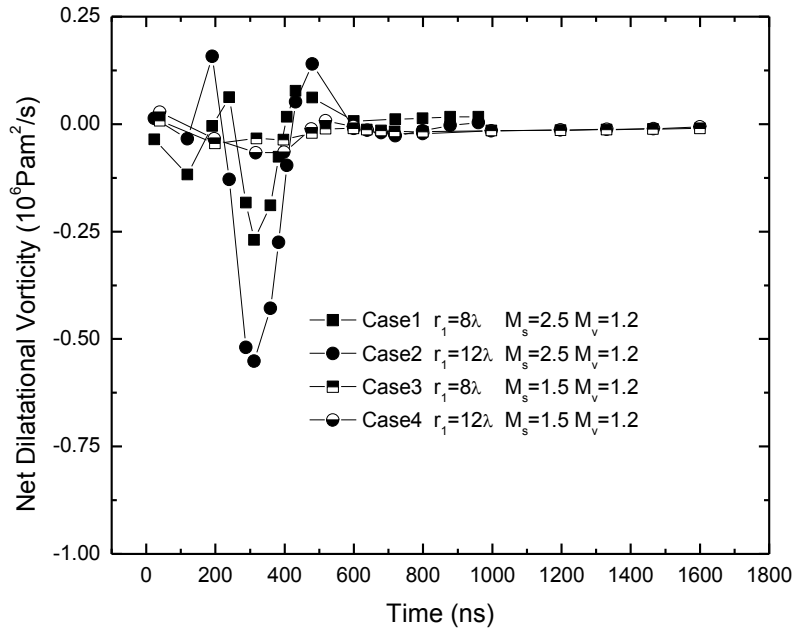
Fig. 20. Time evolution of net dilatational vorticity (cases 1-4).
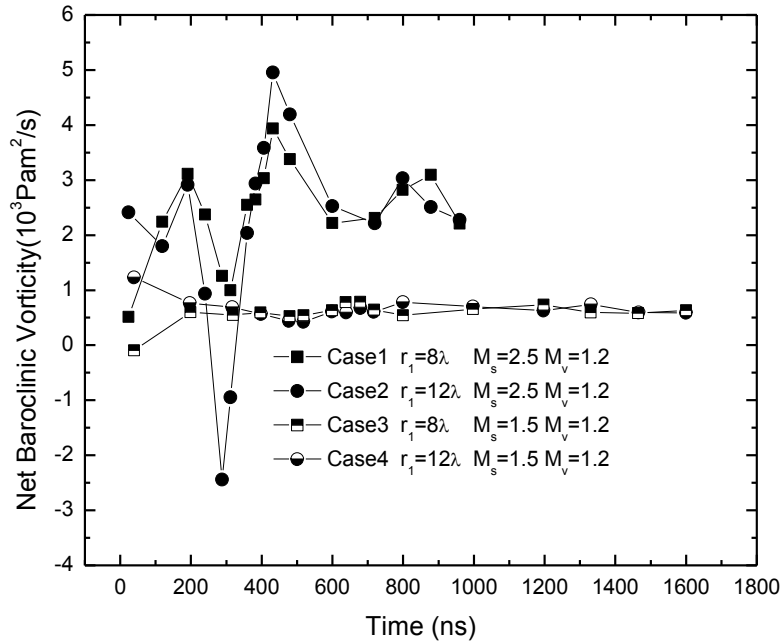
Fig. 21. Time evolution of net baroclinic vorticity (cases 1-4).
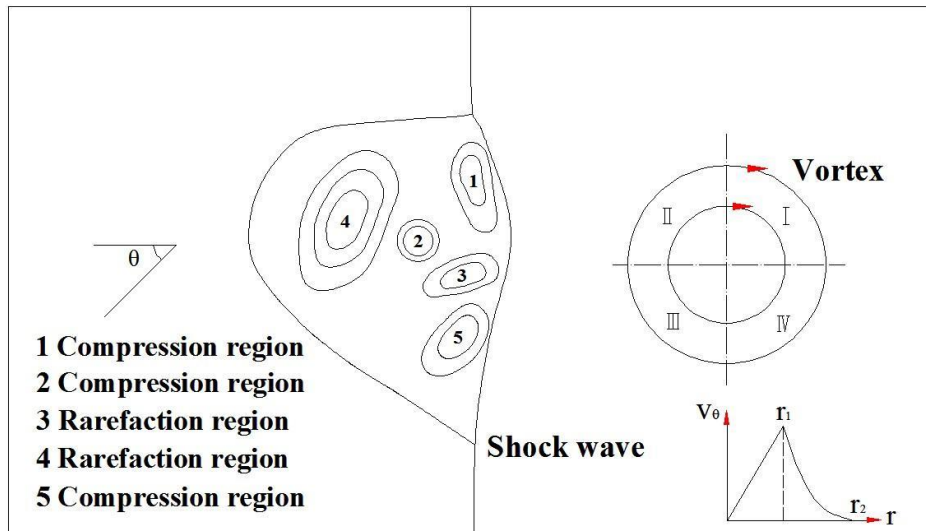
Fig. 22. Physical model of microscale shock-vortex interaction.
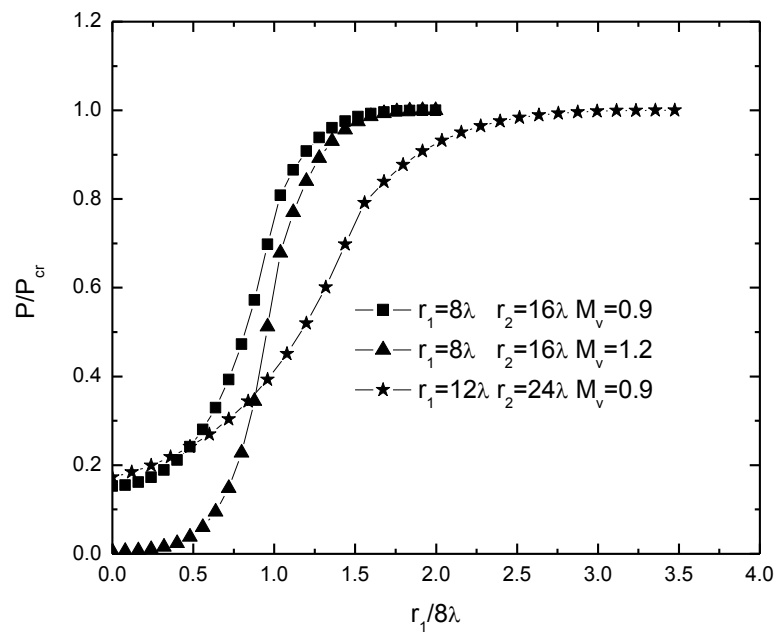
Fig. 23. Pressure distribution in the inner part of composite vortex.
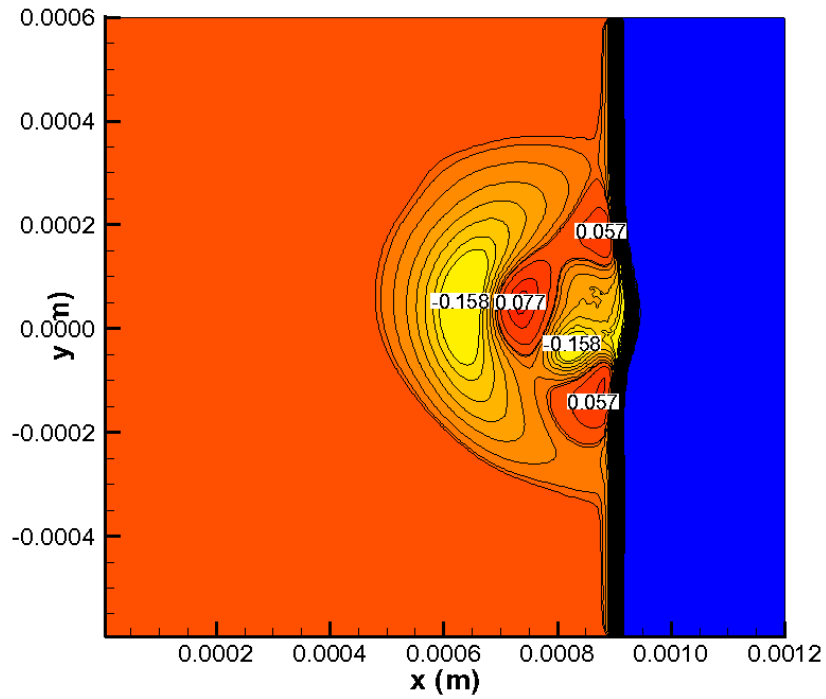
M_S=3.5, M_V=1.2, r=12λ

Fig. 24. Sound pressure contour for case 5.
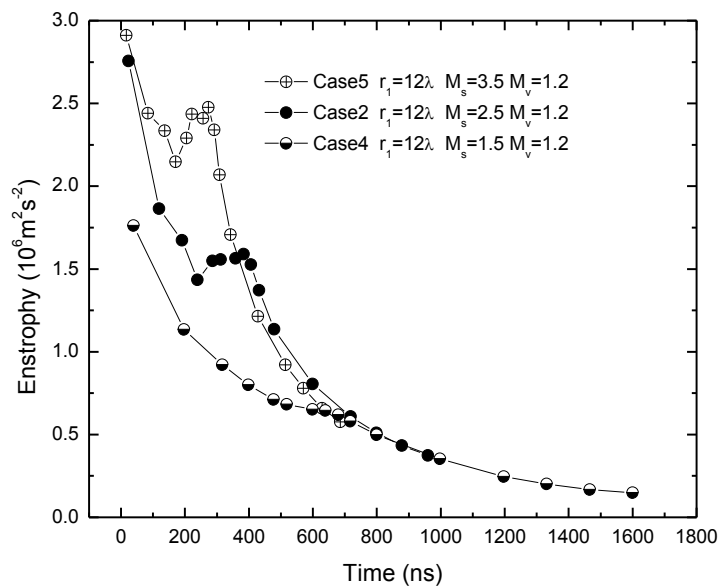
Fig. 25. Time evolution of enstrophy (cases 2, 4, 5)
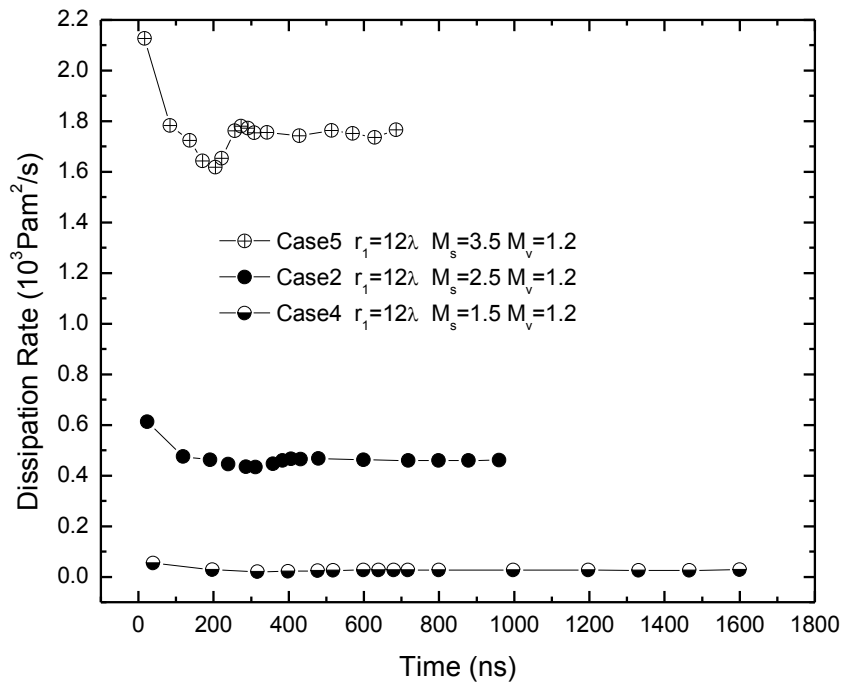
Fig. 26. Time evolution of dissipation rate (cases 2, 4, 5)**.**
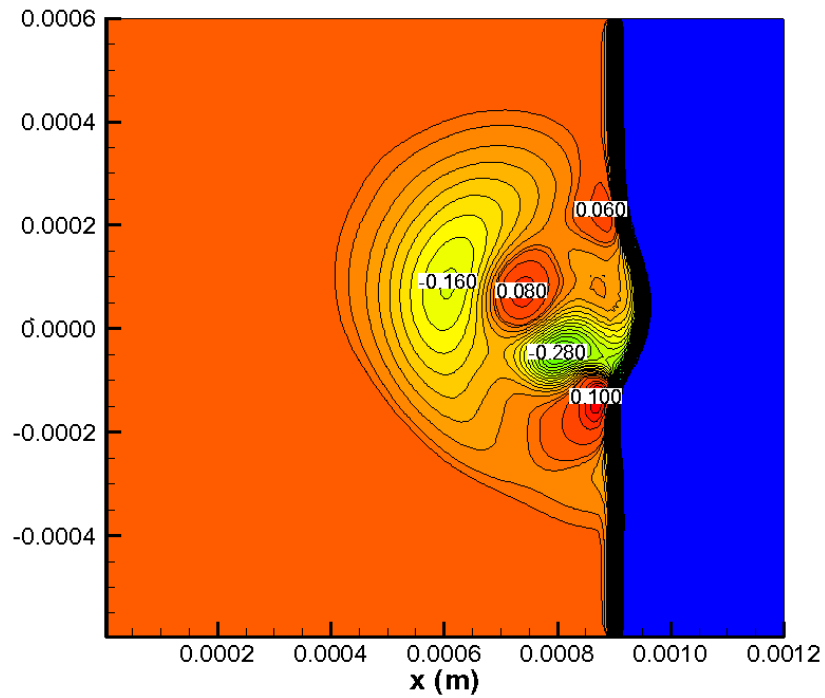
M_S=2.5, M_V=1.2, r_1=16λ

Fig. 27. Sound pressure contour for case 6.
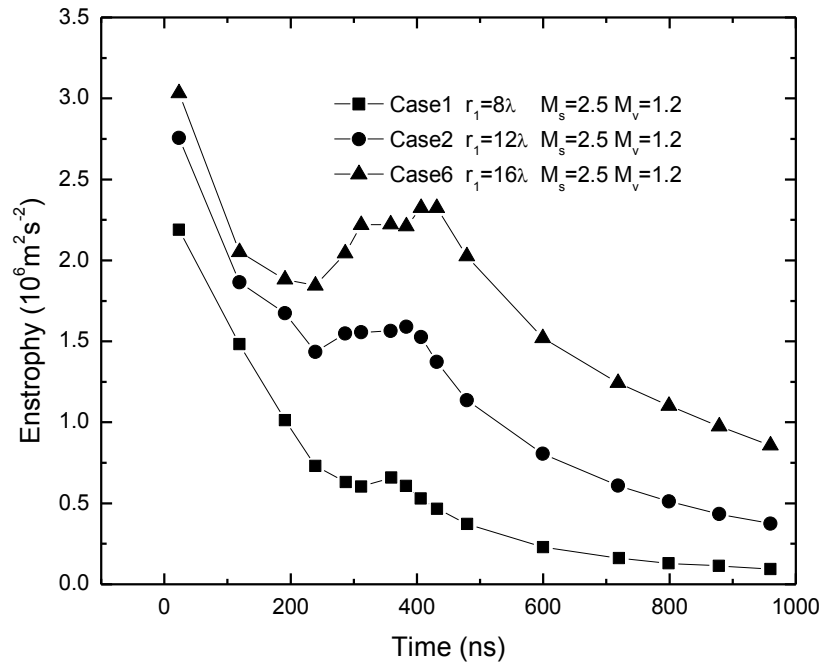
Fig. 28. Time evolution of enstrophy (cases 1, 2, 6).
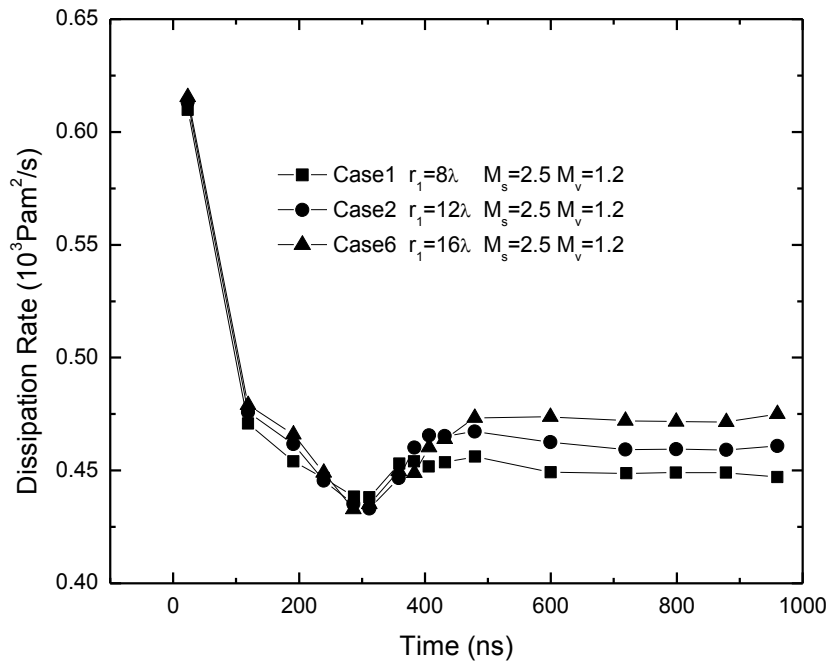
Fig. 29. Time evolution of dissipation rate (cases 1, 2, 6).

43
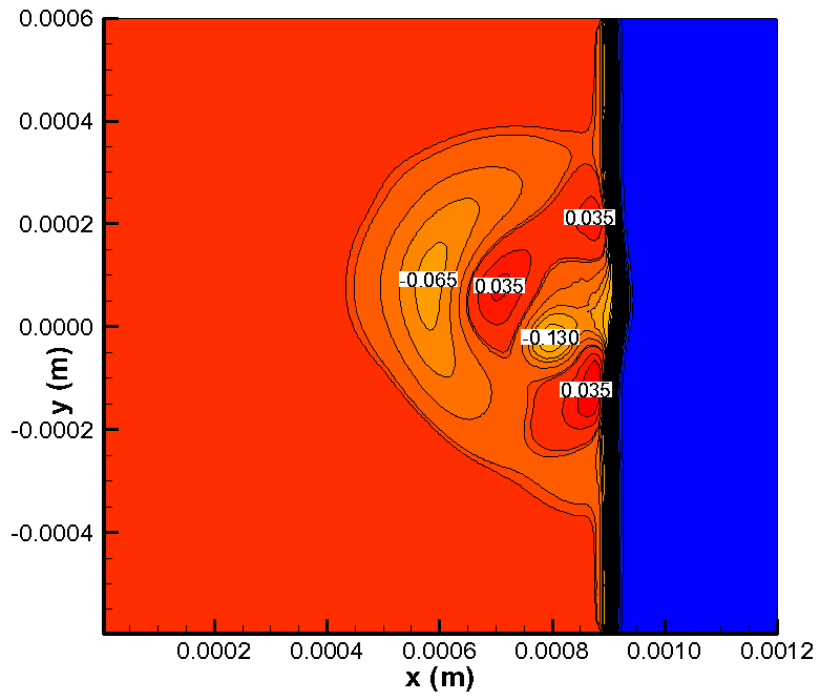
M_S=2.5, M_V=0.9, r_1=12λ

Fig. 30. Sound pressure contour for case 7.
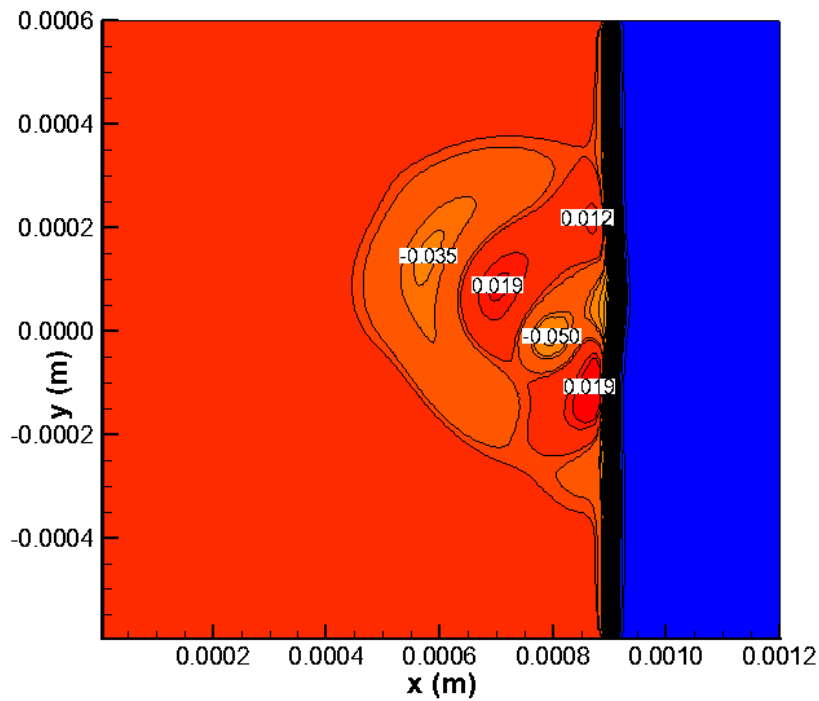
M_S=2.5, M_V=0.6, r_1=12λ

Fig. 31. Sound pressure contour for case 8.
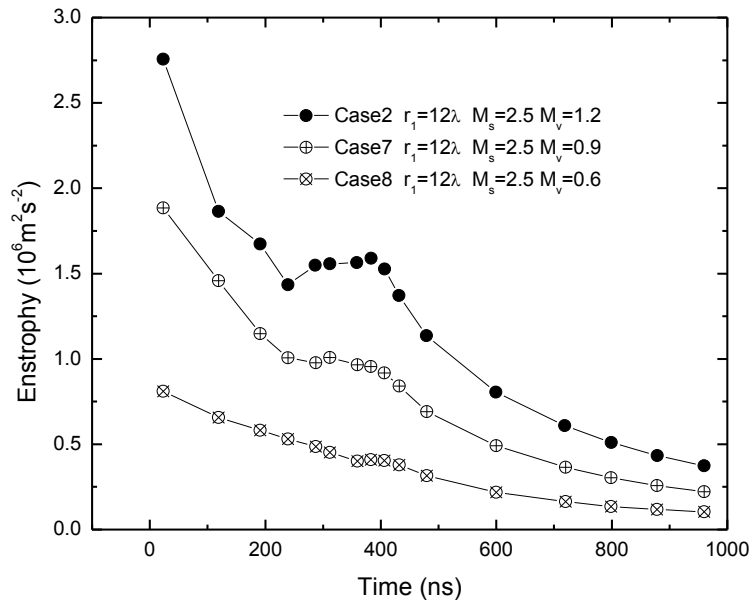
Fig. 32. Time evolution of enstrophy (cases 2, 7, 8).
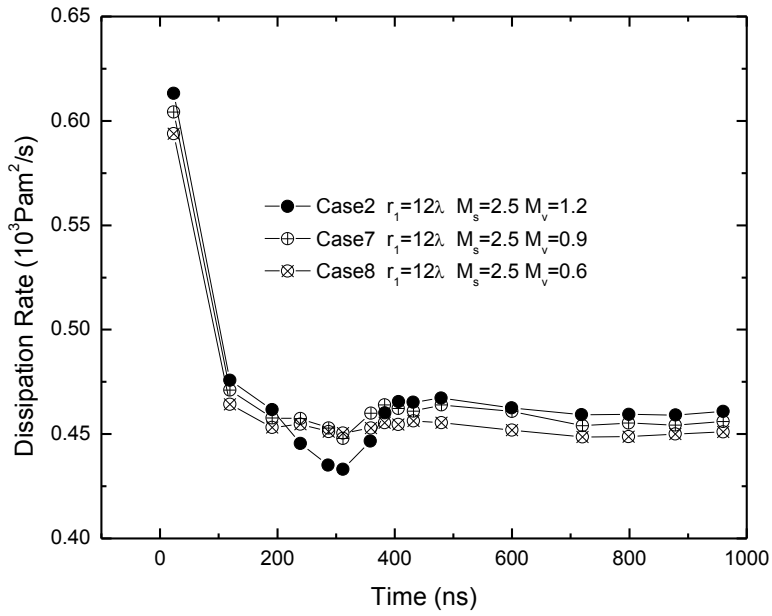
Fig. 33. Time evolution of dissipation rate (cases 2, 7, 8).